

The Diversity of Atomic Hydrogen in Slow Rotator Early-type Galaxies

Lisa M. Young,^{1,2*} Paolo Serra,³ Davor Krajinović,⁴ and Pierre-Alain Duc⁵

¹*Physics Department, New Mexico Tech, 801 Leroy Place, Socorro, NM 87801 USA*

²*Adjunct Astronomer, National Radio Astronomy Observatory*

³*INAF - Osservatorio Astronomico di Cagliari, Via della Scienza 5, I-09047 Selargius (CA), Italy*

⁴*Leibniz-Institut für Astrophysik Potsdam (AIP), An der Sternwarte 16, D-14482 Potsdam, Germany*

⁵*Observatoire Astronomique de Strasbourg, Université de Strasbourg, CNRS, UMR 7550, 11 rue de l'Université, F-67000 Strasbourg, France*

Accepted XXX. Received YYY; in original form ZZZ

ABSTRACT

We present interferometric observations of H I in nine slow rotator early-type galaxies of the ATLAS^{3D} sample. With these data, we now have sensitive H I searches in 34 of the 36 slow rotators. The aggregate detection rate is $32\% \pm 8\%$, consistent with previous work; however, we find two detections with extremely high H I masses, whose gas kinematics are substantially different from what was previously known about H I in slow rotators. These two cases (NGC 1222 and NGC 4191) broaden the known diversity of H I properties in slow rotators. NGC 1222 is a merger remnant with prolate-like rotation and, if it is indeed prolate in shape, an equatorial gas disc; NGC 4191 has two counterrotating stellar discs and an unusually large H I disc. We comment on the implications of this disc for the formation of 2σ galaxies. In general, the H I detection rate, the incidence of relaxed H I discs, and the H I/stellar mass ratios of slow rotators are indistinguishable from those of fast rotators. These broad similarities suggest that the H I we are detecting now is unrelated to the galaxies' formation processes and was often acquired after their stars were mostly in place. We also discuss the H I nondetections; some of these galaxies that are undetected in H I or CO are detected in other tracers (e.g. FIR fine structure lines and dust). The question of whether there is cold gas in massive galaxies' scoured nuclear cores still needs work. Finally, we discuss an unusual isolated H I cloud with a surprisingly faint (undetected) optical counterpart.

Key words: galaxies: elliptical and lenticular, cD — galaxies: evolution — galaxies: ISM — galaxies: structure — Radio lines: galaxies.

1 INTRODUCTION

Recent surveys for cold gas in early-type (elliptical and lenticular) galaxies have found surprising numbers of detections. For example, in a large compilation, Young et al. (2014) found that at least 40% of local early-type galaxies have either atomic gas (H I) or molecular gas (CO), or both, in masses of roughly $10^7 M_{\odot}$ or greater. These cold gas masses correspond to roughly 10^{-4} to 10^{-1} of their total stellar masses. The sample is from the ATLAS^{3D} project (Cappellari et al. 2011a), which is a volume-limited survey of early-type galaxies closer than about 40 Mpc and with stellar masses greater than about $10^{9.9} M_{\odot}$; crucially, the sample is defined with a K_s magnitude cut, which means that the sample is not biased towards younger stellar pop-

ulations. And these relatively high detection rates open up the possibility of using the cold gas as another key to the evolutionary histories of many early-type galaxies.

To make use of this key, it is necessary to know where the cold gas came from. Evidently, sometimes cold molecular gas has cooled and condensed out of a hot X-ray atmosphere (e.g. Lim et al. 2008; Temi et al. 2017). In one recent interesting case, Russell et al. (2017) mapped CO emission in and around the central galaxy of the Abell 1795 cluster. They suggest that relatively low-entropy hot gas was entrained and lifted by rising radio bubbles, and where the hot gas was compressed around the edges of the bubbles, it became thermally unstable and cooled to molecular temperatures. But most early-type galaxies are not the central cluster-dominant or group-dominant members, so additional mechanisms are also needed to explain the majority of the H I and CO-detected early-types. Sometimes kinematic mis-

* E-mail: lisa.young@nmt.edu

alignments between the gas and the stars show that the cold gas was probably acquired relatively late in the galaxy’s history, after the bulk of the stars formed. In those cases the gas could have been accreted from a filament and/or from a cannibalized satellite galaxy. In other cases the cold gas could be recycled (cooled) stellar mass loss material (e.g. Davis et al. 2011; Serra et al. 2014; Negri et al. 2015).

Meanwhile, it is also evident that early-type galaxies come in several different flavors that are believed to have different formation histories (Cappellari 2016). The most massive early-types tend to be slow rotators, spherical or weakly triaxial in shape, and probably formed through a series of gas-poor mergers at the centers of group and cluster halos. Slow rotators at lower masses can also form through major binary mergers that have a particular geometry with a small net angular momentum (see also Bois et al. 2011; Lagos et al. 2017, and references therein). Fast rotators were disc galaxies at high or even moderate redshift, but they have lost a good deal (not necessarily all) of their cold gas and have suffered various disc heating and bulge growth processes as their stellar populations have reddened. Fast rotators can also form through major binary mergers with a particular geometry that gives a high net angular momentum.

In this context, the broad motivation of this project is to make connections between the histories of early-type galaxies as encoded in their stars and in their cold gas. Studies of the quantities and kinematics of cold gas in early-type galaxies can help clarify the nature of the environmental and internal quenching processes that move them towards the red sequence. They can help quantify the potential for rejuvenation episodes, such as the accretion of cold gas and the growth of a young stellar disc in a spheroid-dominated galaxy. And H I in particular often exists at large radii, where it can provide evidence of past interactions for long times (e.g. van de Voort et al. 2015).

Here we present archival and new data on H I emission in nine slow rotator early-type galaxies; with these additions, virtually all of the slow rotators in the volume-limited ATLAS^{3D} survey now have sensitive H I data. In Sections 2 and 3 we describe the selection of targets, the observations, and the data reduction. In Section 4 we provide updated statistics on H I in slow rotators, compare the properties of their H I to fast rotators, and consider some implications for the origin of the gas. In Section 5 we provide some additional notes on the galaxies not detected in H I. In Sections 6 and 7 two galaxies are discussed in more detail, presenting their H I kinematics, its relation to the stellar kinematics and dynamics, and some ideas about whether the galaxies were formed in recent wet mergers or accreted their large gas contents from other sources. Section 8 summarizes this material on H I in slow rotators, and the Appendix presents a basic compilation of H I detections in other spirals and dwarf galaxies that happened to be in the observed fields. One particularly interesting H I detection does not have a known optical companion.

2 SAMPLE

The specific motivation for this project was to obtain more complete information on the H I content of the slow rotators in the ATLAS^{3D} sample. Slow rotators are intrinsically rare,

and relatively few of them have been observed or detected in H I emission. Specifically, the ATLAS^{3D} survey contained a total of 224 fast rotators (Emsellem et al. 2011), of which 111 were observed in H I emission with the WSRT by Serra et al. (2012, hereafter S12) and 41 were detected. The survey also contained 36 slow rotators, of which 21 were observed with WSRT, one was observed with Arecibo, and 9 were detected. The remaining 14 slow rotators were not discussed in S12 because they are at sufficiently low Declination to make WSRT observations difficult or because they are members of the Virgo Cluster.

Analyzing these data, Serra et al. (2014, hereafter S14) found relatively few differences between the H I properties of fast and slow rotators; their H I detection rates, masses, column densities, and morphologies are similar. These similarities are curious and informative because the two types of galaxies probably have very different assembly histories (as mentioned above; Cappellari 2016). However, it is notable that the slow rotator class is internally diverse (Krajinović et al. 2011) and nine H I detections is not a large number. Thus it would be beneficial to assemble the H I information for the remaining slow rotators.

These remaining slow rotators are easily accessible to the NSF’s Karl G. Jansky Very Large Array (VLA), and in some instances they have H I observations from Arecibo. One of them, NGC 4476, has a previously published H I non-detection from the VLA (Lucero et al. 2005). Four of them (NGC 1222, NGC 1289, NGC 5831, and NGC 5846) have archival VLA data which has not been adequately published elsewhere, and it is presented here. Five of them (NGC 4191, NGC 4636, NGC 4690, NGC 5576, and NGC 5813) are newly observed with the VLA and also presented here. In two cases we have obtained H I upper limits from the Arecibo observations of the ALFALFA survey (Giovanelli et al. 2005). The remaining two, NGC 4486 and NGC 4261, will always be difficult for H I emission searches due to their extremely bright radio continuum, though Dwarakanath et al. (1994) discuss H I upper limits in NGC 4486 from a much higher angular resolution absorption experiment.

While the original targets were all slow rotators in the ATLAS^{3D} sample, the clustering nature of galaxies means that some of the ATLAS^{3D} fast rotators and numerous late-type and dwarf galaxies were also present in the observed VLA fields. Table 1 lists the ATLAS^{3D} members that were newly observed at the VLA for this project or retrieved from the archive, and additional information on the late-type and dwarf galaxies is given in Section 4.1 and the Appendix.

3 DATA AND IMAGING

NGC 4191, NGC 4636, NGC 5576, and NGC 5813 were observed with the VLA in October 2015, and NGC 4690 was observed in March 2017. These data were obtained in the D configuration, giving baselines from 0.2 to 5 k λ and resolutions $\sim 55''$; more detailed observing parameters are given in Table 1. The array configuration and time on source were chosen to give beam sizes and sensitivities close to those obtained at WSRT for the other ATLAS^{3D} galaxies. The flux, bandpass, and time-dependent gain calibrations were made following standard procedures, using 3C286 once per observing session as the primary flux and bandpass calibrator, and

secondary gain calibrators were observed every 20 minutes. Calibration was performed using the eVLA scripted pipeline versions 1.3.8 and 1.3.9 in their respective versions of the CASA software package 4.6.0 and 4.7.0. The bootstrapped flux densities of the secondary gain calibrators are in good agreement with previous measurements in the VLA calibrator database and the NRAO VLA Sky Survey (Condon et al. 1998). An initial round of imaging revealed any bright line emission in the data, and the velocities of that emission combined with the known target velocities were used to select frequency ranges for estimating continuum levels. Continuum emission was subtracted using order 0 or 1 fits to the individual visibilities. The final data cubes were produced with a Briggs robustness parameter of 0.5 and cleaned (where necessary) to a residual level of 1 to 1.3 times the rms noise level.

NGC 1222, NGC 1289, NGC 5831, and NGC 5846 were observed in several older VLA projects, as described in Table 1. Observing strategies, data reduction, and imaging are similar to those used for the newer data, except as noted here. The NGC 5846 group, which also includes NGC 5845, NGC 5838, and NGC 5831 from the ATLAS^{3D} sample, plus many late-type galaxies, was observed in a square 36-point mosaic spaced at 15' (the half-power radius of the primary beam). The final image has a gain above 0.90 in a square region 76' on a side, centered on 15h05m47 +01d34m30 (J2000). We note that NGC 5839, also a member of the ATLAS^{3D} sample, is nominally in this field but it falls outside the velocity range covered. To the best of our knowledge, the archival data on NGC 1289 and the NGC 5846 group have not been previously published.

In contrast to all the other data used here, NGC 1222 was observed in the C configuration, giving baselines from 0.3 to 16 k λ and a resolution $\sim 20''$. In addition, only 30 minutes were obtained on source; these data are thus higher resolution and lower sensitivity than the other data discussed in this paper. But as the HI emission is strongly detected, that is appropriate for this target. Thomas et al. (2004a,b) present the total HI flux and HI column density from these data, but they do not discuss the gas kinematics. We have re-reduced the data with slightly higher resolution because we are now able to make comparisons of the HI, CO, ionized gas and stellar kinematics, and that information is not published elsewhere.

The sensitivity, final imaged velocity resolution and velocity coverage of these HI observations are indicated in Table 2. Following the discussion in S12, which uses data of similar sensitivity and resolution, we indicate the HI column density sensitivity as a 5σ signal in one channel of width 16 km s⁻¹ or as close to that as the data will allow. S12 also make a careful analysis of the typical angular sizes and velocity widths of detected HI features in the ATLAS^{3D} survey. Based on this analysis, they adopt M(HI) upper limits for the HI nondetections by calculating the statistical uncertainty in a sum over a data volume of 50 km s⁻¹ and six synthesized beam areas (typically 1.2×10^4 square arcseconds or 110 kpc² to 450 kpc² at the distances of this sample). The mass limit corresponds to three times this formal uncertainty. That procedure is also adopted here. In Section 4.2 we also bring in some upper limits from the Arecibo telescope, and for those data we adopt a mass limit defined by

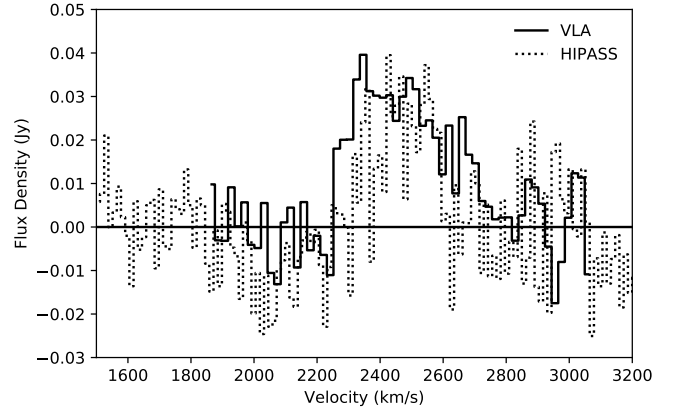


Figure 1. Integrated HI spectrum of NGC 1222, constructed by integrating each channel within a spatial region defined in the column density (moment 0) image. It is compared to the HIPASS spectrum of Doyle et al. (2005), and the two spectra are consistent with each other given the relatively low signal-to-noise ratio and baseline ripples in the HIPASS data.

three times the uncertainty in a sum over 50 km s⁻¹ and one Arecibo beam (3.7×10^4 square arcseconds).

4 RESULTS: HI IN SLOW ROTATORS

4.1 Summary of HI detections and limits

HI emission is detected in NGC 1222 at high signal-to-noise ratio, and more detailed descriptions of the distribution and kinematics are provided in section 6 below. We measure the total line flux from an integrated spectrum (Figure 1) to be $11.2 \pm 0.7 \pm 1$ Jy km s⁻¹, where the 0.7 Jy km s⁻¹ represents the statistical uncertainty due to thermal noise in the data and the 1 Jy km s⁻¹ is a rough estimate of the uncertainty associated with the spatial region of integration. It is notable that the flux recovered in these data is 60% larger than the 6.9 ± 0.8 Jy km s⁻¹ quoted by Thomas et al. (2004a) using the same data. The discrepancy may be due to the choice of data volume to integrate, as the recovered flux density of the gain calibrator B0320+053 is consistent with the NRAO calibrator manual and the 1.4 GHz continuum flux density that we measure for NGC 1222 (61 ± 2 mJy) is consistent with the NVSS value of 62 ± 2 mJy (Condon et al. 1998). For comparison, HIPASS and Effelsberg spectra show HI fluxes of 9.4 Jy km s⁻¹ and 9.5 ± 1.0 Jy km s⁻¹, respectively (Doyle et al. 2005; Huchtmeier & Richter 1989), but both of the single dish spectra suffer from baseline ripples that are probably related to the strong continuum emission.

HI emission is also strongly detected in NGC 4191; the integrated flux density recovered here, 10.1 ± 0.3 Jy km s⁻¹, is also significantly larger than the value of 7.52 Jy km s⁻¹ reported by Courtois & Tully (2015) based on Arecibo data (Haynes et al. 2011). The two spectra are compared in Figure 2. The difference in flux is undoubtedly due to the fact that the extent of the HI emission is larger than the Arecibo beam, and further details on the distribution and kinematics are in section 7.

Table 1. VLA Observations of H I in ATLAS^{3D} galaxies.

Target	Project	Obs. date	Config.	time on source (hr)	Bandwidth (MHz)	Vel. resolution (kHz)
NGC 1222	AT0259	Jul 2001	C	0.5	6.25	97.6
NGC 1289	AR0251	Sep 1992	D	3	6.25	195.3
NGC 4191	15B-258	Oct 2015	D	1.5	16	15.6
NGC 4636	14B-396	Oct 2015	D	1.5	8	1.95
NGC 4690	15B-258	Mar 2017	D	1.5	16	15.6
NGC 5576, 5574	15B-258	Oct 2015	D	1.5	16	15.6
NGC 5813	15B-258	Oct 2015	D	1.5	16	15.6
NGC 5846, 5845, 5838, 5831	AZ0118	Mar 1999	D	36	5.1	97.6

Table 2. H I image properties for Atlas3D galaxies.

Type	Target	Dist. (Mpc)	Vel. range (km s ⁻¹)	beam (")	beam (kpc)	Δv (km s ⁻¹)	rms (mJy/bm)	N(H I) lim (10 ¹⁹ cm ⁻²)	S(H I) (Jy km s ⁻¹)	M(H I) (M _⊙)
(1)	(2)	(3)	(4)	(5)	(6)	(7)	(8)	(9)	(10)	(11)
Slow Rotators	NGC 1222	33.3	1865 – 3060	20 × 15	3.2 × 2.4	21.0	1.15	43	11.2±0.7	(2.9±0.2)×10 ⁹
	NGC 1289	38.4	2206 – 3466	77 × 50	14 × 9.3	42.0	0.40	2.4	< 0.13	< 4.7×10 ⁷
	NGC 4191	39.2	1132 – 4172	49 × 45	9.3 × 8.6	16.0	0.70	2.7	10.1±0.3	(3.7±0.1)×10 ⁹
	NGC 4636	14.3	143 – 1663	51 × 45	3.5 × 3.1	16.0	0.70	2.7	< 0.15	< 7.0×10 ⁶
	NGC 4690	40.2	1216 – 4264	70 × 50	14 × 9.7	16.0	0.80	2.0	< 0.16	< 6.3×10 ⁷
	NGC 5576	24.8	–4 – 3020	54 × 46	6.5 × 5.5	16.0	0.65	2.3	< 0.14	< 2.0×10 ⁷
	NGC 5813	31.3	421 – 3453	51 × 46	7.7 × 7.0	16.0	0.67	2.5	< 0.14	< 3.2×10 ⁷
	NGC 5831	26.4	1324 – 2367	57 × 50	7.3 × 6.4	22.0	0.48	2.0	< 0.12	< 1.9×10 ⁷
NGC 5846	24.2	1324 – 2367	57 × 50	6.7 × 5.8	22.0	0.48	2.0	< 0.12	< 1.6×10 ⁷	
Fast Rotators	NGC 5574	23.2	–4 – 3020	54 × 46	6.1 × 5.2	16.0	0.65	2.3	< 0.14	< 1.7×10 ⁷
	NGC 5838	21.8	1324 – 2367	57 × 50	6.0 × 5.3	22.0	0.48	2.0	< 0.12	< 1.3×10 ⁷
	NGC 5845	25.2	1324 – 2367	57 × 50	7.0 × 6.1	22.0	0.48	2.0	< 0.12	< 1.8×10 ⁷

Distances are taken from Cappellari et al. (2011a). The velocity range in column 4 indicates the usable range covered by the data.

Column 7 gives the channel widths in the image cubes used for analysis; for the newer data, these are significantly wider than the intrinsic resolution of the data. The column density limit represents 5σ in one channel and the integrated flux density limit represents three times the statistical uncertainty in a sum over 6 beams and 50 km s⁻¹.

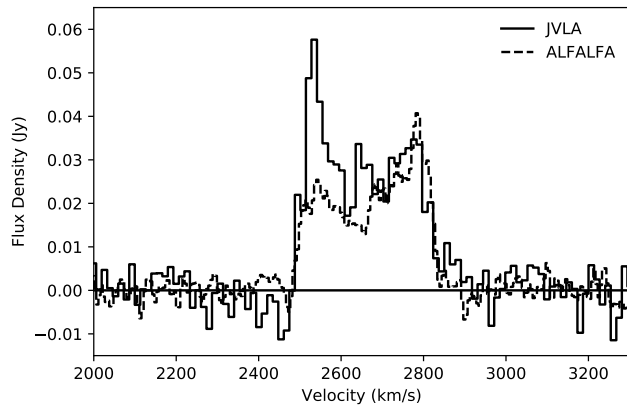


Figure 2. Integrated H I spectrum of NGC 4191, constructed by integrating each channel within a spatial region defined in the column density (moment 0) image. It is compared to the Arecibo spectrum of Haynes et al. (2011), which misses most of the blue peak because the disc extends beyond the Arecibo beam on the North side of the galaxy.

No emission is found in the other ATLAS^{3D} targets, giving the mass limits in Table 2. To the best of our knowledge, these are the first published H I observations of NGC 1289, NGC 4690, NGC 5813, NGC 5831, and NGC 5845. There are previous single-dish nondetections of NGC 4636, NGC 5574, NGC 5576, NGC 5838, and NGC 5846 (Duprie & Schneider 1996; Huchtmeier & Richter 1989), though our new limits are considerably more sensitive. A few additional comments about these H I non-detections are provided in Section 5.

In the field of NGC 5576 we do, however, detect significant emission from the spiral galaxy NGC 5577, and we find another H I detection whose optical counterpart is faint and not currently identified. In the field of NGC 4690 we find emission from UGC 07945. In the field of NGC 5813 we find emission from NGC 5806, NGC 5811, and UGC 09661, and in the large mosaic of the NGC 5846 group there are H I detections from six galaxies. Additional information on those detections is in the Appendix, and good upper limits could also be obtained for a large number of other objects in the mosaic field.

4.2 Updated statistics on H I in slow rotators

Table 3 presents the updated compilation of H I masses or upper limits in the ATLAS^{3D} slow rotators. Interferometric

observations from WSRT or the VLA are now available for 31 of the 36 slow rotators. Three others have HI upper limits from Arecibo. NGC 4261 also has Arecibo observations from the ALFALFA survey, but its bright continuum emission makes the noise level at least a factor of 10 higher than for the other galaxies and we do not count it as useful data. The continuum issue also plagues HI observations of NGC 4486, as mentioned in Section 2 above.

We thus have sensitive, reasonably high resolution HI observations of 34 slow rotators and HI detections in 11 of them (0.32 ± 0.08 , for a 68% confidence interval). Outside of the Virgo Cluster, we have observations of 26 slow rotators and 10 detections (0.38 ± 0.10).¹ The new detection rates in slow rotators have dropped by approximately 1 standard deviation compared to those reported in S14, because the newly compiled observations are preferentially nondetections. Indeed, it seems probable that one could expect older but previously unpublished data to be largely nondetections because of a publication bias.

Completing the sample (or nearly so) gives much improved constraints on the incidence of HI in slow rotators, as the previous data left open the possibility that the HI detection rate of slow rotators could be much (up to a factor of 2) higher than that of the fast rotators. Instead, the new results imply that the HI detection rates of slow rotators are virtually indistinguishable from those of fast rotators. For specific examples, the overall HI detection rate in the fast rotators in S14 was 0.31 ± 0.05 , comparable to the updated rate in slow rotators of 0.32 ± 0.08 . Considering only the galaxies outside of the Virgo Cluster, S14 reported an HI detection rate of 0.37 ± 0.06 for fast rotators and that value is in good agreement with the rate of 0.38 ± 0.10 for slow rotators.

As an aside, we note that Cappellari (2016) proposes a slightly modified definition of the slow rotator class from the one we have adopted here. Four of the 260 ATLAS^{3D} galaxies have different classifications in the two systems. In the modified definition, three of the slow rotators in Table 3 would become fast rotators. These are NGC 3796, NGC 4550, and NGC 4690. One new slow rotator would be added to Table 3; it is NGC 4733. None of these are detected in HI emission and the HI detection statistics would therefore not change significantly.

4.3 Additional comparisons of HI properties in fast and slow rotators

There are several other ways in which the new data emphasize the similarities in the HI properties of fast and slow rotators. For example, S14 found that there were no small HI discs (HI class *d*, for discs of similar size to the stellar body) among slow rotators. NGC 1222 now fills this niche (Section 6). The incidence of relaxed HI discs in slow rotators outside of the Virgo Cluster is now 6/26 or 0.23 ± 0.09 , in good agreement with the analogous rate 0.25 ± 0.05 for fast rotators. The data in S14 also suggested a dearth of slow rotators at the highest HI masses; specifically, Figures 2 and 5 in S14 show several fast rotators with HI/stellar mass ratios $\log M(\text{HI})/M_\star \approx -1$, but no such gas-rich slow

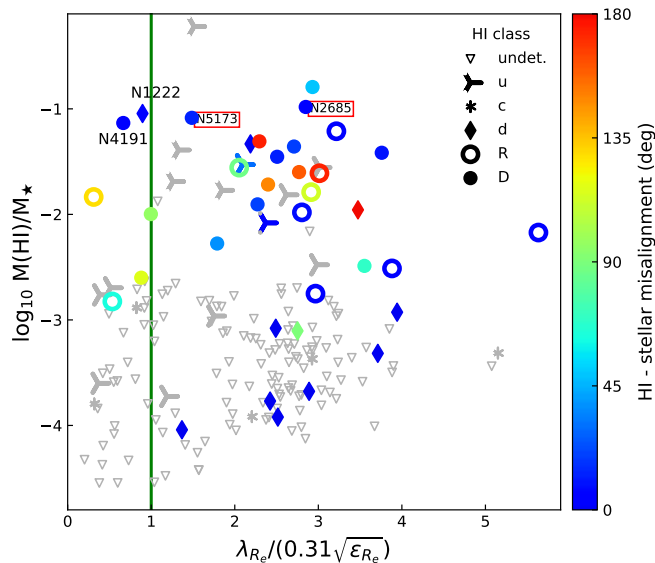


Figure 3. An updated version of Figure 5 from S14. HI masses in the ATLAS^{3D} sample are plotted against a scaled version of the stellar specific angular momentum parameter λ_{R_e} . Slow rotators are located to the left of the vertical line and fast rotators are to the right. The symbol shapes indicate the HI morphology: *u* are unsettled distributions like tails or streams, *c* are small clouds, *d* are small discs, *D* are large discs, and *R* are rings. The symbol colours indicate the kinematic misalignments between the HI and the stars, as in S14. Gray symbols mean that HI is not detected or that it is not settled enough for the misalignment angle to be meaningful. NGC 5173 and NGC 2685 are also marked because their dramatic kinematic twists are not adequately captured by the median misalignment value.

rotators. NGC 1222 and NGC 4191 have stellar masses $\log M_\star = 10.50$ and 10.70 , respectively (Cappellari et al. 2013), and their HI masses give them $\log M(\text{HI})/M_\star = -1.04$ and -1.13 . These values fill in the apparent gap in those figures so that slow rotators reach the same high levels of HI richness as fast rotators (Figure 3). The new HI detections are also found in low density environments, as well (several local density estimates are given in Cappellari et al. 2011b), consistent with the trend noted in S12.

There is one other facet of the new data that provides a perspective beyond the results of S14, and that is the HI kinematics and its alignment with respect to the stars. S14 focused on those alignments as indicators of the evolutionary connections (or the lack thereof) between gas discs and stellar discs. Very simply, if a stellar disc forms out of a gas disc, the systems should share kinematics. But unlike spirals, early-type galaxies frequently show strong misalignments between their gas and stellar systems. Davis et al. (2013) discuss misalignments between stars and molecular/ionized gas, and Lagos et al. (2015) provide some possible interpretations of those misalignments. Molecular gas is very rare in slow rotators, though (Young et al. 2011), so the HI misalignments are more interesting for slow rotators, at least in the cases where the HI is relaxed into a regular disc. S14 found only two cases of slow rotators with both well-defined HI and stellar kinematics, and in both of these cases

¹ The Virgo Cluster slow rotator detected in HI is NGC 4406.

the H I is roughly polar (90° misalignment).² There are two other cases with well-defined H I kinematics but poorly constrained stellar kinematics, and those are also polar if one assumes the objects are oblate so that the photometric axis is a proxy for the kinematic axis.³ Thus, the evidence from S14 suggested that H I in slow rotators is most commonly in a polar configuration, when it is sufficiently relaxed to be in a long-lived configuration.

In contrast, in NGC 1222 and NGC 4191 the H I and stars rotate about nearly identical axes. They still have interesting structural features, though; NGC 1222 (Section 6) exhibits prolate-like rotation in its stellar body, so while its gas kinematics are closely aligned with its stellar kinematics, it may have an uncommon shape. NGC 4191 (Section 7) takes the more common oblate shape, but it is also one of the unusual “ 2σ ” galaxies consisting of two coplanar but counterrotating stellar discs (Krajnović et al. 2011). Therefore, its H I corotates with one of the stellar discs but counterrotates relative to the other. In short, the new data present examples of H I-rich slow rotators with aligned stellar and H I kinematics. Figure 3 shows how these two compare to the other slow and fast rotators in terms of their H I masses, kinematics and morphologies; it reinforces the similarities between the H I properties of slow rotators and fast rotators.

The simulations of S14 and Lagos et al. (2015) have convincingly shown that gas kinematics in early-type galaxies are sensitive indicators of the galaxies’ evolutionary histories, so improved simulations should attempt to reproduce the full spectrum of shapes, structures, and misalignments exhibited by early-type galaxies.

4.4 Discussion: Implications for the formation of slow rotators

Cappellari (2016) has summarized the formation processes of slow rotators as falling in two broad categories, one of which takes place in clusters and groups (dense environments) and the other of which takes place in the field. The first category includes scenarios such as a brightest cluster galaxy disrupting and accreting other cluster members, and after many such mergers, a relaxed cluster can contain one enormous slow rotator that is well-separated from other cluster members in the mass-size plane. In less relaxed clusters, where substructure is present, there may be multiple slow rotators associated with the sub-groups; however, these should eventually merge as well. In the field, however, the formation of slow rotators is expected to be more of a stochastic process which happens when the orbital configuration of a major merger is “just right” to produce a remnant with very low specific angular momentum. This latter process can also produce relatively small, low-mass slow rotators, and it can produce dispersion-dominated galaxies as well as rotation-dominated galaxies whose *net* angular momentum is low because they contain two counter-rotating structures.

In this context, the fact that the H I content of slow rotators matches that of fast rotators is probably related to the overall H I content of the universe at low redshift. Both fast

and slow rotators can form in mergers, some of which may be gas-rich, and both can accrete cold gas from their surroundings, if there is any cold gas in the vicinity. Of course there is still a very strong dependence of H I content on the local galaxy density, as noted by S12 and confirmed here. Thus we might not expect the most massive slow rotators in galaxy clusters to have H I.

Additional evidence for a variety of formation paths for early-type galaxies comes from their nuclear structures: specifically, the presence or absence of inner cores in the surface brightness profiles. Scouring by an inspiraling supermassive black hole binary is a popular model for the formation of cores, though not the only model (Krajnović et al. 2013b). It is also generally expected that it should be much more difficult to form or maintain a core when cold gas is present. The dissipational nature of the cold gas should make it sink towards the nucleus and form stars, refilling the scoured core. And as discussed by Krajnović et al. (2013b), cored galaxies are commonly slow rotators and core-less galaxies are commonly fast rotators, though there are exceptions to those rules.

In this context, with our updated statistics on the H I content of slow rotators, we reassess possible links between their cold gas content and their nuclear structure. Table 4 presents data on H I and CO detections in the ATLAS^{3D} galaxies with nuclear surface brightness classifications. We first note that detections of H I emission are slightly more common in cored than in core-less slow rotators; H I is detected in 4 of 13 cored slow rotators and one of nine core-less slow rotators. However, it is useful to remember that much of that H I emission is in the outskirts of the galaxies. Gas in the “c” or “u” morphologies, i.e. irregular clouds or unsettled distributions, may never have been close enough to the nucleus to refill a scoured core. Thus, we also tabulate detections of *central* H I or CO emission on kpc scales, where we find cold gas present in 3 of 9 core-less slow rotators but in only one of the 13 cored slow rotators.

This relatively simple association suffers, of course, from small number statistics, but the picture is also complicated by the fact that the data are inhomogenous in quality and several of the cored slow rotators are also detected in other species. The CO detection in NGC 4374 corresponds to $(6\pm 1)\times 10^6 M_\odot$ of cold molecular gas (Boizelle et al. 2017), and we should note that it comes from ALMA data of much higher sensitivity and resolution than that available for any other galaxy in the table. Furthermore, NGC 4486, NGC 4636, and NGC 5813 are detected in the [O I] 63 μm line, in their central kpc or so, and this line is usually associated with the outer envelopes of molecular clouds (Section 5). NGC 4261 and NGC 4374 are also detected in the mid-IR lines of excited H_2 (Ogle et al. 2010), giving masses in the range of 10^5 to $10^7 M_\odot$ of molecular gas at temperatures of a few hundred K. This CO, H_2 and neutral O could represent gas that has cycled through an AGN feedback episode of the type described by Russell et al. (2017). The FIR and mid-IR spectroscopy data are only available for a few early-type galaxies, so it is difficult to make broader conclusions about the incidence of these species, and it is also not clear whether these detections represent gas that is capable of star formation (filling in the cores).

In short, cored galaxies are detected in H I emission on large scales at a similar or higher rate as core-less galax-

² These are NGC 3414 and NGC 5631.

³ These are NGC 3522 and UGC 03960.

Table 3. Updated data on H I in ATLAS^{3D} slow rotators.

Name	Slow/Fast $R_e; R_e/2$	Kin. Type	class	core?	log M(H I) (M_\odot)	log M(H I)/ M_\star	H I morph	Notes	source	Virgo Cluster
(1)	(2)	(3)	(4)	(5)	(6)	(7)	(8)	(9)	(10)	(11)
NGC0661	S S	NRR/CRC	c	...	< 7.37	< -3.56	S12	
NGC1222	S S	NRR/NF	b	...	= 9.46	= -1.04	d	...	*	
NGC1289	S S	NRR/CRC	c	...	< 7.67	< -3.05	*	
NGC3414	S S	NRR/CRC	c	\	= 8.28	= -2.83	D	P,R,L	S12	
NGC3522	S S	NRR/KDC	c	...	= 8.47	= -1.83	D	P,R	S12	
NGC3608	S S	NRR/CRC	c	∩	= 7.16	= -3.80	c	...	S12	
NGC3796	S S	NRR/2s	d	\	< 7.10	< -2.89	S12	
NGC4168	S S	NRR/KDC	c	∩	< 7.46	< -3.84	S12	
NGC4191	S S	NRR/2s	d	...	= 9.57	= -1.13	D	W,L	*	
NGC4261	S S	NRR/NF	b	∩	
NGC4365	S S	NRR/KDC	c	∩	< 7.52	< -4.01	α	
NGC4374	S S	NRR/LV	a	∩	< 7.26	< -4.33	S12	V
NGC4406	S S	NRR/KDC	c	∩	= 8.00	= -3.60	u	...	S12	V
NGC4458	S S	NRR/KDC	c	∧	< 6.91	< -3.12	S12	V
NGC4472	S S	NRR/CRC	c	∩	< 7.23	< -4.54	α	V
NGC4476	S F	RR/NF	e	∧	< 7.29	< -2.71	L05	V
NGC4486	S S	NRR/LV	a	∩	V
NGC4528	S F	NRR/2s	d	\	< 7.18	< -2.94	S12/ α	V
NGC4550	S S	NRR/2s	d	∧	< 6.89	< -3.51	S12	V
NGC4552	S S	NRR/NF	b	∩	< 6.87	< -4.33	S12	V
NGC4636	S S	NRR/LV	a	∩	< 6.85	< -4.55	*	
NGC4690	S S	NRR/NF	b	...	< 7.80	< -2.82	*	
NGC5198	S S	NRR/NF	b	∩	= 8.49	= -2.70	u	...	S12	
NGC5322	S S	NRR/CRC	c	∩	< 7.34	< -4.19	...	A	S12	
NGC5481	S S	NRR/KDC	c	...	< 7.21	< -3.40	S12	
NGC5557	S S	NRR/NF	b	∩	= 8.57	= -2.76	u	...	S12	
NGC5576	S S	NRR/NF	b	∧	< 7.30	< -3.58	*	
NGC5631	S F	NRR/KDC	c	...	= 8.89	= -2.00	D	M,W,L	S12	
NGC5813	S S	NRR/KDC	c	∩	< 7.51	< -4.08	*	
NGC5831	S S	NRR/KDC	c	\	< 7.28	< -3.59	*	
NGC5846	S S	NRR/LV	a	∩	< 7.20	< -4.37	*	
NGC6703	S F	NRR/LV	a	\	< 7.18	< -3.80	S12	
NGC7454	S S	NRR/NF	b	...	< 7.16	< -3.47	S12	
PGC028887	S F	NRR/KDC	c	...	= 7.65	= -2.88	c	...	S12	
PGC050395	S S	NRR/CRC	c	...	< 7.51	< -2.63	S12	
UGC03960	S F	NRR/NF	b	...	= 7.79	= -2.60	D	W,L	S12	

These are the ATLAS^{3D} galaxies classified as slow rotators based on stellar kinematics within one effective radius (R_e). Column 2 gives the fast/slow classifications within R_e and $R_e/2$ from [Emsellem et al. \(2011\)](#). Columns 3 and 4 give the stellar kinematic types and classes from [Krajnović et al. \(2011\)](#). Kinematic type abbreviations are as follows: RR = regular rotator; NRR = non-regular rotator;

CRC = counterrotating core; KDC = kinematically decoupled core; LV = low velocity core; 2s = two velocity dispersion peaks, symptomatic of counterrotating discs; NF = no other distinguishing features. The kinematic classes in column 4 are more general. Class a includes those galaxies without detected rotation in the field; class b galaxies have complex velocity fields not otherwise classified.

Class c galaxies have kinematically distinct cores, d galaxies have two counterrotating discs, and e galaxies have simple aligned rotation. Column 5 gives the nuclear structure classification from [Krajnović et al. \(2013b\)](#), as ∩ = core, ∧ = intermediate, and \ = power law. Columns 6 to 9 give the H I mass, H I to stellar mass ratio, morphology and kinematic notes. Stellar masses are taken from [Cappellari et al. \(2013\)](#). From [Serra et al. \(2012\)](#), the H I morphological classes in column 8 are as follows: u = unsettled, such as tails or streams; c = clouds, small and irregular; d = small disc; D = large disc. Further H I kinematic notes in column 9 include these: A =

H I detected (also) in absorption; L = lopsided; M = H I misaligned relative to the stellar kinematics; P = polar orientation ($\approx 90^\circ$ misalignment); R = ring; W = warp. The H I reference is in column 10, with a key as follows. S12 = [Serra et al. \(2012\)](#); * = this paper; L05 = [Lucero et al. \(2005\)](#); α = the ALFALFA survey ([Giovanelli et al. 2005](#)), and R. Giovanelli, private communication. Column 11 indicates Virgo Cluster membership according to [Cappellari et al. \(2011a\)](#).

ies; they are not commonly detected in H I emission in their nuclei, but they are occasionally detected in other species associated with cold atomic and/or molecular gas. In any case it is clear that the issue of star-forming gas and stellar cores requires more work.

5 NOTES ON THE H I NON-DETECTIONS

Broadly speaking, the H I detection rate in early-type galaxies is only 32% (S12), so the many non-detections in the current set is not surprising. But in some cases we have additional information about other phases of the interstellar medium and the environment of our targets, and this in-

Table 4. Cold gas and cores in slow rotators.

	H I	no H I	Total	central H I or CO
Core-less	1 3414 (D)	8 3796, 4458, 4476, 4528, 4550, 5576, 5831, 6703	9	3 3414, 4476, 4550
Core	4 3608 (c), 4406 (u), 5198 (u), 5557 (u)	9 4168, 4365, 4374, 4472, 4552, 4636, 5322, 5813, 5846	13	1 4374

The table lists the number of galaxies in each category and their NGC identifiers. For H I-detected galaxies, the H I morphological classification from S12 is also given. This table includes only the ones with *both* published core/core-less status (Krajinović et al.

2013b) and good H I and CO data. Thus NGC 4486 and NGC 4261, both cored galaxies, are not listed because they lack good H I data. Central H I data are taken from Young et al. (2014) and CO data from Young et al. (2011) and Crocker et al. (2009), with a recent CO detection of NGC 4374 from Boizelle et al. (2017).

formation can help place the non-detections into a broader context.

For comparison to the H I upper limits, we note that FIR photometry from the Herschel Reference Survey gives estimated dust masses for two of these galaxies. Smith et al. (2012) find $\log M_d (M_\odot) = 5.06 \pm 0.19$ for NGC 4636 and < 5.51 for NGC 5576. Adopting a $M(\text{H I})/M_d$ ratio of 100, based on empirical correlations from the other members of the Herschel Reference Survey (Cortese et al. 2016), the dust limit for NGC 5576 is consistent with our H I non-detection. The nominal $M(\text{H I})/M_d$ ratio suggests that we should have detected $10^7 M_\odot$ of H I in NGC 4636, but that is not a compelling inconsistency given the large range in observed $M(\text{H I})/M_d$ ratios. The other HRS galaxies exhibit values from 10 to 1000, and two other ATLAS^{3D} slow rotators (NGC 3414 and NGC 4406) have $M(\text{H I})/M_d$ ratios of 100 and 23, respectively. Thus it would not be unusual to have $M(\text{H I})/M_d < 100$ in NGC 4636 and the HI nondetection could still be consistent with the dust detection.

Besides dust masses, we note that NGC 4486, NGC 4472, NGC 4636, NGC 5813, and NGC 5846 are detected in [C II] 158 μm emission (Brauhar et al. 2008; Werner et al. 2014). In nearby late-type galaxies, [C II] emission is usually associated with cold molecular gas as it should form a photodissociated envelope on the UV-exposed skin of a molecular cloud. But of course it can also arise in ionized gas, and in fact Wilson et al. (2013) have suggested that the [C II] emission in the early-type galaxy NGC 4125 should be entirely attributed to ionized gas. In this context it is not obvious whether the [C II] detections mentioned above should lead us to expect H I or CO detections. But there are also [O I] 63 μm detections in NGC 4486, NGC 4636, and NGC 5813, and these are unambiguously associated with neutral atomic or molecular gas. Further quantitative analysis should be carried out to check whether the simultaneous detections of [O I] and the non-detections of H I in NGC 4636 and NGC 5813 are significant. The [O I] detections do serve as a reminder that significant quantities of cold gas can be hiding beneath the present sensitivity limits.

Finally, it is notable that NGC 5576 and NGC 5574 are undergoing a strong interaction, and NGC 5574 has developed impressive tidal tails (Figure 4). Evidently NGC 5574 has been relatively poor in cold gas for some time, as there is no stripped H I in the tails. Strong H I emission from the spiral NGC 5577 could cause confusion in single dish HI observations of the region, though. The system is discussed in more detail in the Appendix.

6 COLD GAS IN THE MERGER REMNANT NGC 1222

NGC 1222 is a well-known recent merger remnant, currently undergoing starburst activity. New, deep optical observations from Duc et al. (2015) clearly show several shells and tails (Figure 5). It is evidently in a merger-driven star formation episode, and given its star formation rate (Davis et al. 2014) its gas consumption time is 1 to 2 Gyr. On that kind of a timescale we would thus expect the optical features to fade and the cold gas content to decline as it approaches the structure and appearance of the other slow rotators. At present, though, it is unique among the slow rotators in being the only one detected in both H I and CO emission; its HI/H₂ mass ratio of 2.4 ± 0.4 is similar to typical values found in fast rotators, whereas slow rotators tend to be H₂-poor (Young et al. 2014). The H I and CO emission are coincident with a dust lane, with the CO emission nestled into a central depression in the H I column density, and the gas and dust are all oriented roughly perpendicular to the stellar photometric major axis. The previous literature on the galaxy has not discussed the H I kinematics and its relation to the merger features, so we present that information here.

6.1 Prolate-like rotation in gas and stars

In more detail, the structure of the galaxy can be quantified by applying the kinemetry routines of Krajinović et al. (2006) to the deep *g* image and velocity fields. Regions interior to a radius of $30''$ in the optical image are strongly disturbed by dust and areas of recent star formation activity. Exterior to that, the photometric position angle shows a gentle twist from -60° at $30''$ to -10° at radii of $200''$. The outer isophotes are again strongly distorted by the shells and tails. For comparison, within the SAURON field of view the stellar kinematic PA is found to be $43.0^\circ \pm 9.2^\circ$ (Krajinović et al. 2011), so that the stellar rotation is nearly about the photometric major axis. This long-axis or prolate-like rotation suggests that the stellar body of the galaxy may have a prolate or triaxial shape.

The gas kinematics are also roughly aligned with the stellar kinematics (Figure 5). We estimate the kinematic PA of the ionized gas to be $63^\circ \pm 11^\circ$; that of the H I to be $48.5^\circ \pm 1.3^\circ$; and that of the CO to be $40^\circ \pm 2^\circ$. The systematic trend in position angle, from ionized gas through H I to CO, is suggestive that the gas (having been disturbed in the merger) is settling towards a stable plane as it cools. On the other hand it is notable that both the H I and CO are lumpy, so the true uncertainties on the PAs may be larger than the values formally suggested by the statistical analysis. In short, in NGC 1222 the stellar rotation is prolate-like, and all the gas kinematic PAs are a close match to the stellar

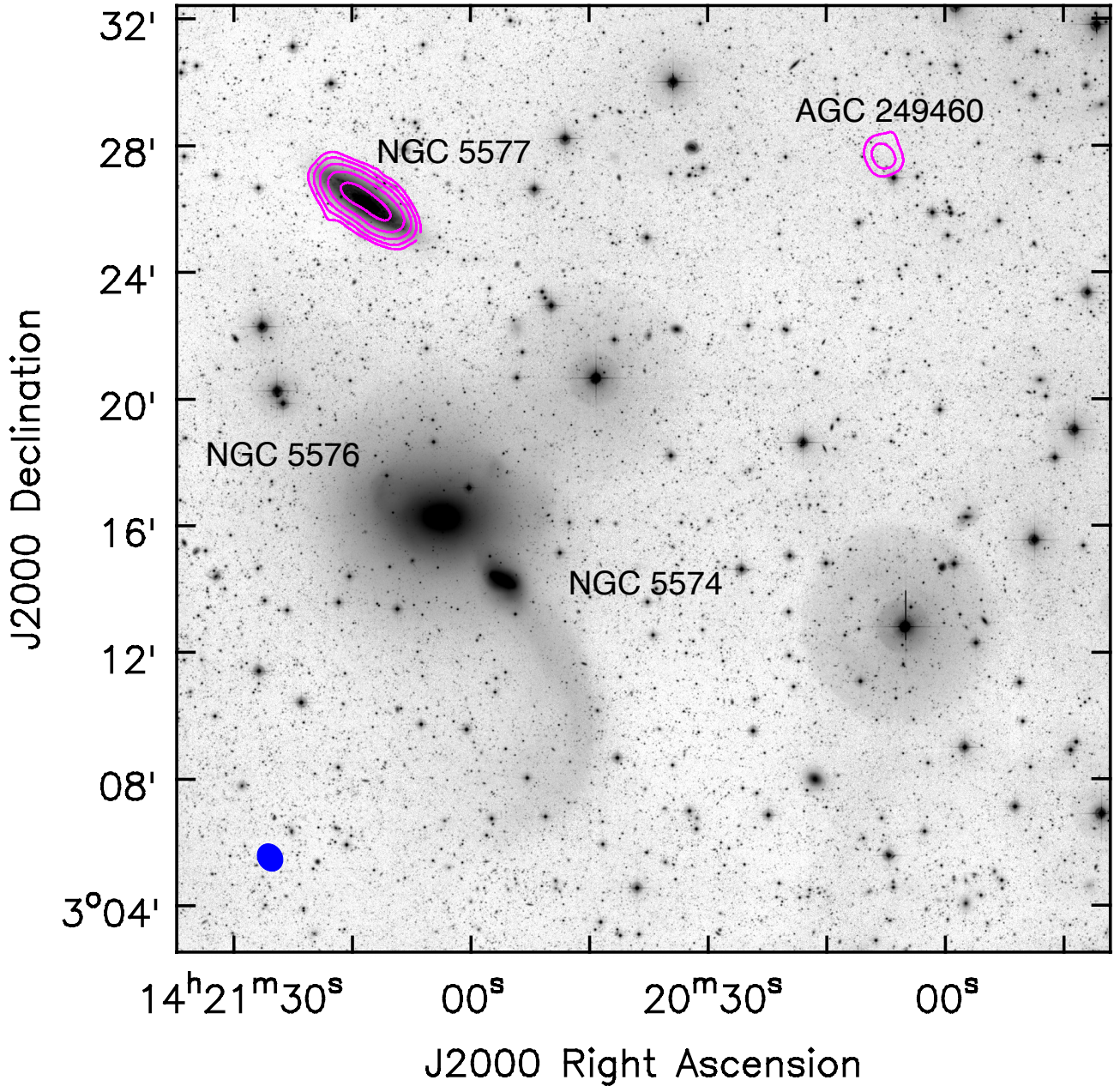


Figure 4. The NGC 5577, NGC 5576, and NGC 5574 group. The optical image is the MATLAS g data; the H I column density image is overlaid, and contours are $(3, 6, 12, 24, 48) \times 2.3 \times 10^{19} \text{ cm}^{-2}$. A primary beam correction has been applied to the H I column densities. The blue ellipse in the bottom left corner indicates the H I resolution. AGC 249460 is discussed in the Appendix.

kinematic PA. If the galaxy is indeed prolate then the gas is close to its equatorial plane.⁴ After it has aged and reddened, NGC 1222 may look like NGC 5485, another ATLAS^{3D} galaxy with prolate-like rotation and a dust disc along its photometric minor axis (kinematic major axis). Of course, a

recent merger like NGC 1222 may not yet have approached its final stable configuration, so it is difficult to infer its true shape. Stellar kinematics at larger radii would also be helpful for determining whether the prolate-like rotation persists farther out.

Kinematic analysis of the H I velocity field also indicates that at moderate radii ($10''$ to $40''$), where the velocity field is well behaved, the inclination of the H I disc is $38^\circ \pm 6^\circ$. With this inclination, the inferred rotation speed in the H I disc is $162 \text{ km s}^{-1} \pm 20 \text{ km s}^{-1}$. The dynamical mass

⁴ In this case, despite the superficial similarities, the structure of NGC 1222 is different from that of NGC 5128 (Cen A). Sparke (1996) shows that NGC 5128 appears to be an oblate galaxy with a polar disc.

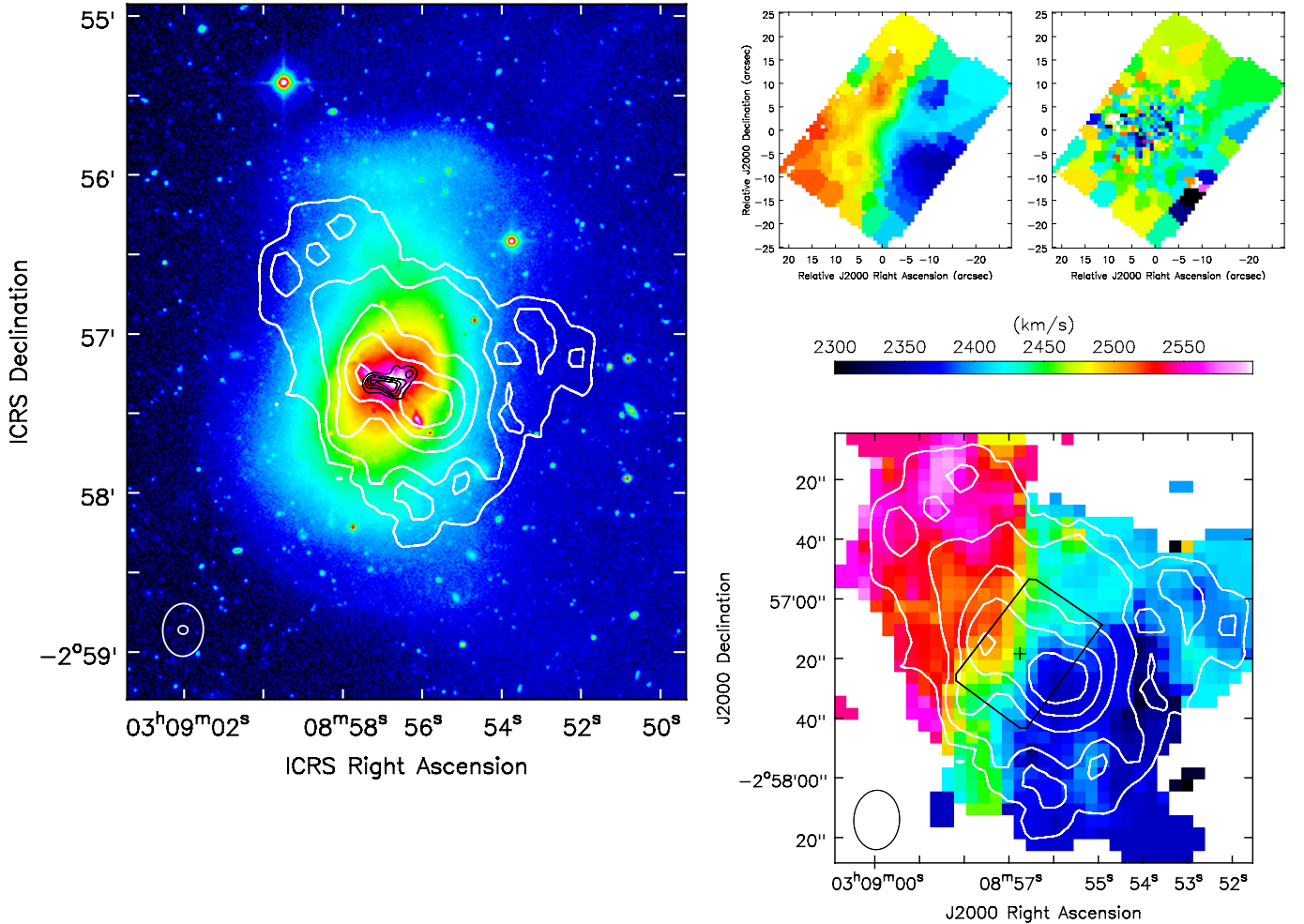


Figure 5. NGC 1222. Left: Optical is the g-band MATLAS image from [Duc et al. \(2015\)](#). White contours show the H I distribution; contours are (0.1, 0.2, 0.4, 0.6, 0.8) times the peak, which is $1.14 \text{ Jy beam}^{-1} \text{ km s}^{-1}$ or $4.1 \times 10^{21} \text{ cm}^{-2}$. Black contours show the CO distribution from [Alatalo et al. \(2013\)](#); they are (0.2, 0.4, 0.6, 0.8) times the peak value of $17.5 \text{ Jy beam}^{-1} \text{ km s}^{-1}$ or $4.2 \times 10^{22} \text{ molecules cm}^{-2}$ at a conversion factor of $3 \times 10^{20} \text{ molecules cm}^{-2} \text{ per (K km s}^{-1})$. Right: Velocity fields in NGC 1222. The lower image shows H I velocities; the black cross marks the optical nucleus and the black polygon shows the field of view for the optical velocity data. The upper pair are the [O III] velocities (left) and the stellar velocities (right). All the velocity fields use the same colour scale.

interior to $40''$ (6.5 kpc) is then $4.0 \times 10^{10} M_{\odot}$, which is consistent with the dynamical mass of $3.2 \times 10^{10} M_{\odot}$ inferred by [Cappellari et al. \(2013\)](#) from stellar kinematics. Given the irregular HI distribution at larger radii, dynamical masses might not be reliable further out; in any case, there is no strong evidence of dynamical inconsistency.

6.2 Tails, shells, and the formation of NGC 1222

Like NGC 1222, many of the ATLAS^{3D} galaxies exhibit stellar shells and tails at low surface brightness; two-thirds of the ones imaged deeply by [Duc et al. \(2015\)](#) have such features. From this perspective NGC 1222 may be something like a younger version of NGC 5557, which was studied in more detail by [Duc et al. \(2011\)](#). In NGC 5557, diffuse H I emission is clearly associated with a remarkable long stellar tail, and the galaxy is interpreted as the remnant of a major gas-rich merger. That merger probably drove a great deal of

cold gas to the center of the galaxy, but the central gas has since been consumed, and H I only remains out in the stellar tail where the dynamical timescales are long. In contrast to NGC 5557, we detect no H I emission associated with the stellar tails and shells in NGC 1222, though it should be noted that the sensitivity of these VLA data is not as good as the WSRT data for NGC 5557. At the sensitivity of the NGC 1222 data, we would have detected H I like that in the shells of NGC 5128 and similar shell galaxies ([Schiminovich et al. 1994, 1995, 2013](#)), but we would not have detected the faint clouds near NGC 5557. Thus, since the H I and CO in NGC 1222 are not obviously aligned with or associated with the stellar tails and shells, it's not clear whether the cold gas took part in the event that formed the stellar features. It could have been accreted afterwards. Deeper H I observations and more careful analysis of the stellar populations in the shells could help to clarify the nature of the recent merger that formed NGC 1222.

In this regard, NGC 1222 is also interesting for its comparison to numerical simulations of galaxy formation. [Li et al. \(2018\)](#) have studied the merger histories of prolate galaxies in the Illustris simulation, and they find their prolate galaxies were primarily formed in a major dry merger with a radial geometry. [Tsatsi et al. \(2017\)](#) also describe a merger that forms a prolate galaxy, but again it is a dry merger. If these kinds of collisionless merger scenarios describe the history of NGC 1222, then the cold gas presumably was accreted after the merger. Strictly speaking we should note that these analyses focus on galaxies with stellar masses $M_{\star} > 10^{11} M_{\odot}$, but NGC 1222 ($M_{\star} \sim 3.2 \times 10^{10} M_{\odot}$) is not far below the range studied. On the other hand, [Li et al. \(2018\)](#) also find two cases of prolate galaxies formed through mergers where one progenitor had 10–15% of its baryonic mass in the form of gas. [Ebrova & Lokas \(2017\)](#) identify several other cases in the Illustris simulation in which gas-rich mergers formed massive galaxies with prolate-like rotation. As NGC 1222 currently has $M(\text{HI}+\text{H}_2)/M_{\star} \sim 0.13$, this gas-rich merger scenario might also be roughly appropriate for it.

7 AN UNUSUALLY LARGE HI DISC IN NGC 4191

Amongst the ATLAS^{3D} slow rotators in Table 3, NGC 4191 is unusual for having the largest HI mass and disc diameter. Its HI mass and diameter are, in fact, in league with the properties of nearby spirals. It was classified by [Krajnović et al. \(2011\)](#) as a “two σ -peak” galaxy, meaning that it consists of two superposed, dynamically cold, counterrotating stellar discs, and these galaxies are often found to be slow rotators because the two discs’ rotations interfere destructively in the mean velocity field. Its rotational kinematics were also studied in more detail by [Coccatto et al. \(2015\)](#). Despite these interesting kinematics, a deep optical image ([Duc et al. 2015](#)) shows little evidence for extended, low-surface brightness features like tails or shells. Its unusual HI disc, in combination with its counterrotating stellar discs, make it particularly interesting for studies of the gas kinematics in comparison to the stellar kinematics.

7.1 HI distribution and kinematics

The HI in NGC 4191 is clearly peaked on the optical galaxy nucleus, with a peak column density of $3.6 \times 10^{20} \text{ cm}^{-2}$ at this 9 kpc spatial resolution (Figure 6). HI column densities are high in a bright elongated ridge which is approximately $3.3'$ (38 kpc) in diameter and is poorly resolved in the minor axis direction. This ridge is surrounded by an extended disc of column density $\approx 1.2 \times 10^{20} \text{ cm}^{-2}$, extending to a radius of $6'$ (68 kpc) on the north side and $4'$ (45 kpc) on the south side. The outer disc is asymmetric, having higher column densities on the south side but a larger physical extent on the north side.

We employ the kinematic analysis of [Krajnović et al. \(2006\)](#) to describe the HI velocity field, and the results are in Figures 7 and 8. Figure 7 presents the observed velocity field, the modeled field and the residuals. Figure 8 presents the radial variation in the kinematic parameters of the disc – its orientation, inclination, circular velocity and deviations from

circular velocity. We find that at all radii unaffected by beam smearing (outside the FWHM), the projected circular velocity k_1 is approximately constant at $140 \text{ km s}^{-1} \pm 5 \text{ km s}^{-1}$. Here the error estimate describes the dispersion about the mean, rather than the uncertainty in the mean. The inclination of the HI disc can be estimated from the axis ratio parameter q , for which we find a median value of 0.72 and a dispersion of 0.05. Assuming a thin disc, the inclination of the HI is $44^\circ \pm 4^\circ$ and the deprojected circular velocity is then $202_{-14}^{+18} \text{ km s}^{-1}$. The most prominent kinematic feature in the HI disc is a twist in kinematic PA, which changes from 200° at radii of $60''$ to $90''$ (11 to 17 kpc) to 180° at radii $> 150''$ (28 kpc). Fitting the full three-dimensional HI data cube with the 3DBarolo software ([Di Teodoro & Fraternali 2015](#)) reproduces all these results, with a slightly larger inclination $49^\circ \pm 4^\circ$ and correspondingly lower rotation velocity $184 \pm 12 \text{ km s}^{-1}$. The inner kinematic PA of 200° matches the photometric major axis of the HI ridge to within a few degrees and the location of the kinematic twist matches the end of the ridge. This twist is apparently not associated with a significant change in the inclination.

7.2 Stellar structure and ionized gas kinematics

For comparison to the stellar structure of the galaxy, we have also applied the kinemetry routines to a deep g -band image of NGC 4191. The image was obtained as part of the MATLAS project ([Duc et al. 2015](#)). Figure 9 shows the fitted stellar isophote parameters as a function of the semi-major axis length. The galaxy has a very regular structure with a slight position angle twist from 10° at a radius of $8''$ to 0° at $90''$, and the stellar kinematic axis is consistent with the photometric axis (at least in the inner parts, where both can be measured; [Krajnović et al. 2011](#)). The isophote axis ratio has a minimum of 0.67 at radii between $10''$ and $20''$, increasing to 0.80 outside of that range. These values are entirely consistent with those found by [Coccatto et al. \(2015\)](#) from SDSS data, though we are able to trace the structure nearly a factor of 2 farther in radius. We also find mildly discy isophotes ($b_4 > 0$), which, together with the axis ratio dip, is undoubtedly due to the influence of the stellar disc that is described by [Coccatto et al. \(2015\)](#) as the secondary or inner stellar disc.

The stellar isophotal axis ratio of NGC 4191 is relatively large, especially in comparison to other 2σ galaxies. If NGC 4191 is an oblate fast rotator, as is argued elsewhere for the 2σ galaxies, and if we adopt the intrinsic axis ratio 0.25 ± 0.14 for fast rotators ([Weijmans et al. 2014](#)), then the *minimum* apparent stellar axis ratio of 0.67 implies an inclination angle of 50_{-2}^{+4} degrees.

A kinematic analysis of the ionized gas velocity field from [Coccatto et al. \(2015\)](#) is also shown in Figure 9. The ionized gas kinematic PA is a close match to the stellar photometric PA at radii $\sim 12''$ to $30''$. The gas’s kinematic axis ratio q is smaller than the stellar photometric axis ratio, as one would expect when the gas disc is thinner than the stellar body. The annuli for radii $7''$ to $30''$ give the ionized gas axis ratio to be $q = 0.56 \pm 0.13$, which corresponds to an inclination of 56_{-10}^{+8} degrees. The inclination of the ionized gas disc is thus consistent with suggestions from the stellar isophote axis ratios.

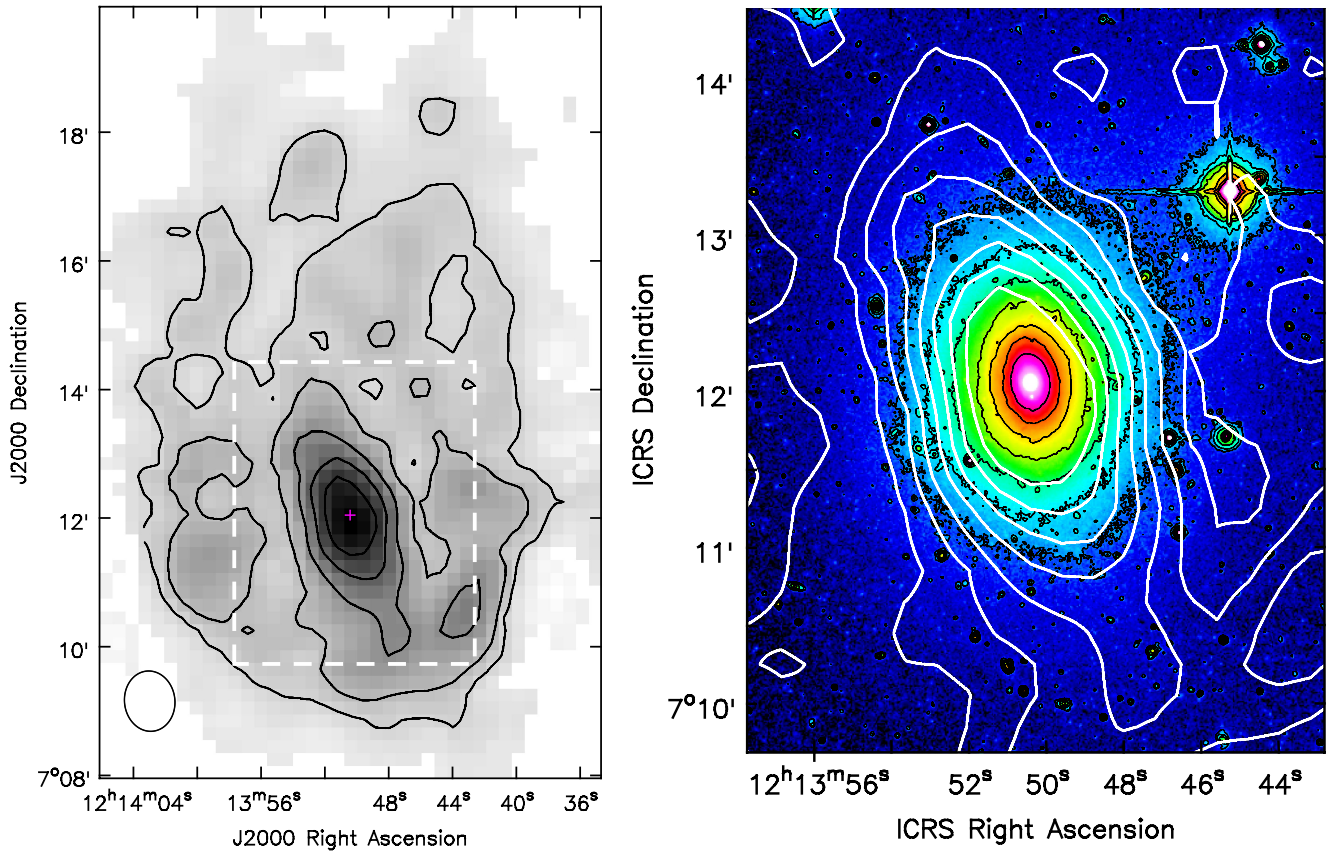


Figure 6. H I distribution in NGC 4191; the left panel shows the column density in greyscale and contours, with contours at (0.1, 0.2, 0.4, 0.6, and 0.8) times the peak, which is $0.876 \text{ Jy beam}^{-1} \text{ km s}^{-1}$ or $3.6 \times 10^{20} \text{ cm}^{-2}$. A small magenta cross marks the optical nucleus, and the white box marks the region displayed in the right panel. On the right, the H I distribution (white contours) is overlaid on the MATLAS g image (colour and black contours, which are spaced at a factor of 2 in surface brightness).

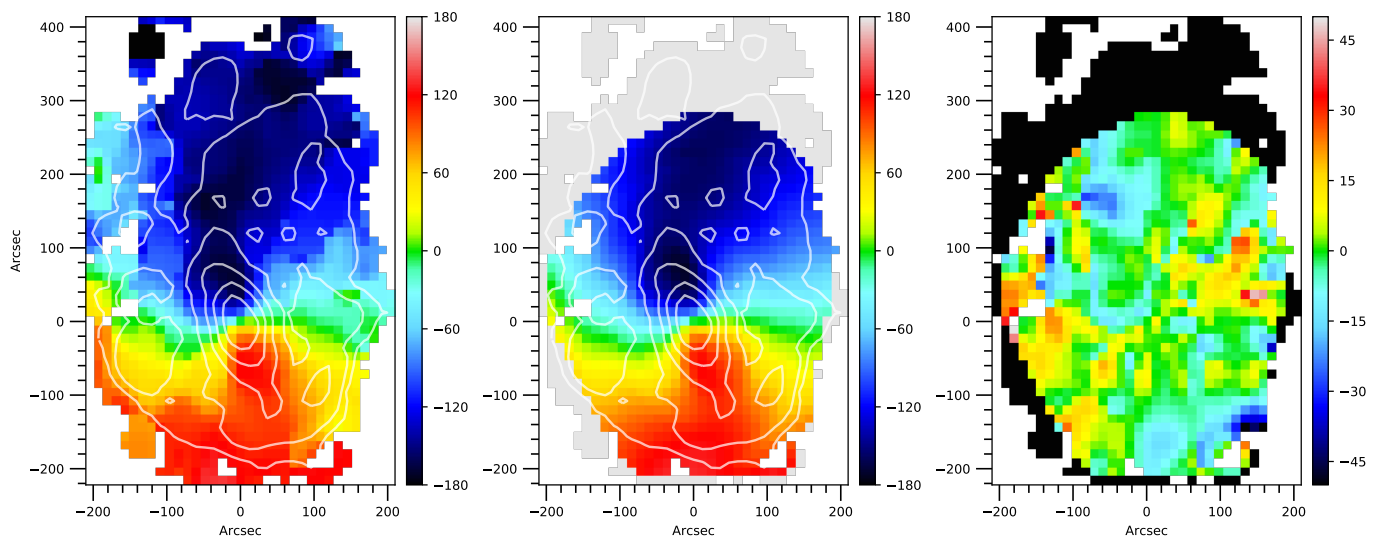


Figure 7. H I kinematics in NGC 4191. Left: H I velocity field, the input for the kinemetry. The velocity field was formed by fitting a Gaussian to the spectrum at each pixel. Column density contours, from Figure 6, are overlaid in white. Center: reconstructed kinematic model velocity field. Right: residuals. Each panel also has a colour wedge indicating velocities in km s^{-1} .

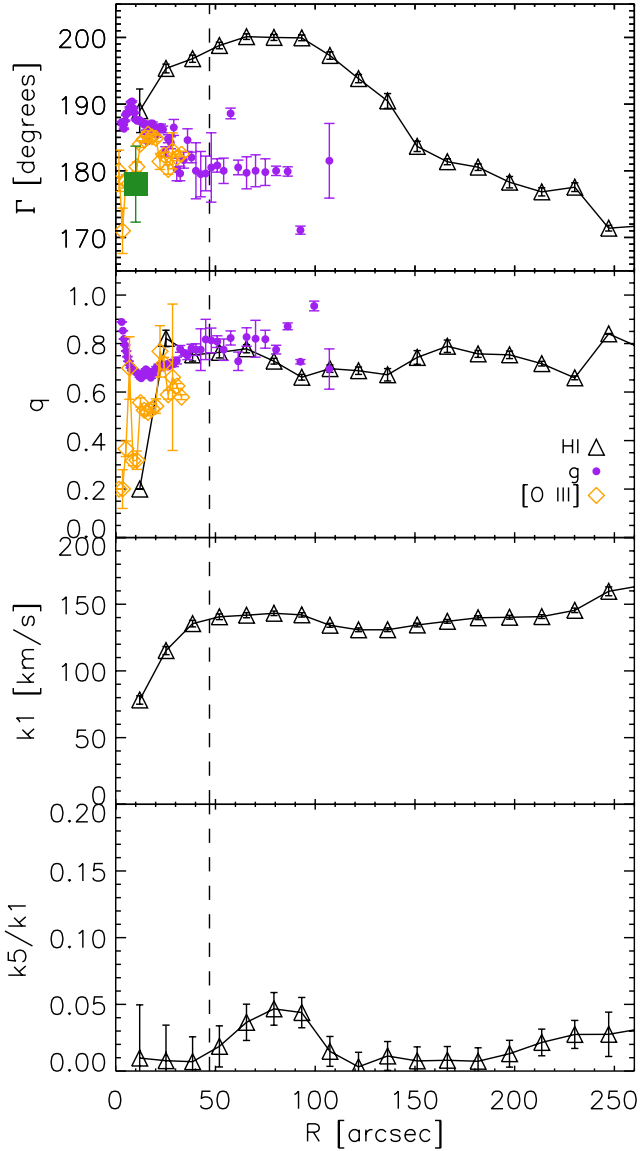


Figure 8. Kinematic analysis on the HI velocity field in NGC 4191 (black triangles). The parameter Γ is the position angle of the major axis, and q is the ellipse axis ratio. In the case of a thin, inclined disc with pure circular rotation, the parameter k_1 is equivalent to the projected velocity $V_c \sin i$; k_5 indicates deviations from simple circular rotation. The dashed vertical line indicates the HI resolution (FWHM), so values interior to this radius will be severely affected by beam smearing. Purple symbols indicate the stellar photometric position angle and axis ratio, from Figure 9; orange symbols show [O III] kinematics; and the green symbol indicates the kinematic position angle of the ionized gas in the SAURON field of view (Davis et al. 2011).

7.3 H I disc vs. stellar discs

The H I kinematic major axis is 20° offset from the stellar photometric major axis over the radius range $40'' - 90''$, where we have good measurements in both bands and the H I velocity field is still very regular. Thus, the misaligned H I kinematic axis suggests that the H I at radii $\lesssim 150''$ (28.5 kpc) may be precessing. The orbital timescale at that ra-

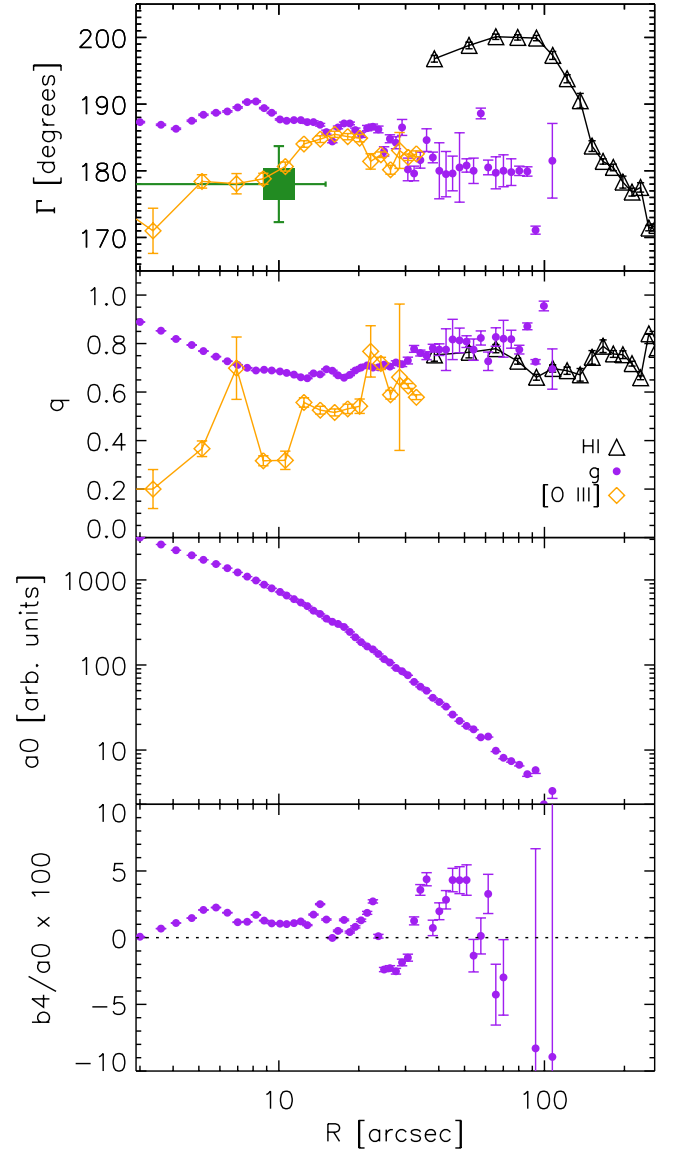


Figure 9. Photometric analysis on the deep MATLAS g image of NGC 4191. Symbols are as in Figure 8, and Γ and q are again the ellipse major axis position angle and axis ratio. The parameter a_0 is the stellar surface brightness and b_4/a_0 indicates the amplitude of the $\cos 4\theta$ component in a Fourier decomposition of the surface brightness. Boxy isophotes have $b_4 < 0$ and discy isophotes have $b_4 > 0$ (Jedrzejewski 1987). The ionized gas kinematics for radii less than about $7''$ may be biased, due to a large mask for a foreground star.

dus is 870 Myr, and it might be tempting to associate that timescale with a proposed merger or accretion event (see Section 7.5 below), but at present we cannot make a specific attribution with any known event in the galaxy's history. In terms of the broader context, though, a 20° misalignment is mild compared to many misalignments and twists noted in S14 and Morganti et al. (2006), and it would not have been notable without such high quality optical data and relaxed outer isophotes.

Another point of interest is that the inclination of the

H I disc, which we infer to be $44^\circ \pm 4^\circ$ or $49^\circ \pm 4^\circ$, is consistent with values inferred from ionized gas kinematics and stellar isophotes. Dust features at radii out to $\sim 20''$ in an HST F814W image are also broadly consistent with this lower inclination. But it is very different from the 90° inferred by Cappellari et al. (2013) from Jeans anisotropic modeling of the stellar kinematics. Thus the gaseous disc of NGC 4191 seems to be kinematically quite distinct from the stellar structures at radii $\lesssim 30''$. Higher resolution H I data could help to show whether the H I disc is strongly warped and twisted on scales too small to resolve in the current data.

For context, again, we note that the evidence for a moderate inclination in NGC 4191 makes it different from most of the other 2σ galaxies in the ATLAS^{3D} sample. The other 2σ galaxies all have JAM inclinations greater than 57° , which is not surprising as it should be much easier to detect the double-disc kinematic signature when the discs are closer to edge-on (Krajnović et al. 2011). But the other 2σ galaxies do not have large cold gas discs, so in those cases we lack the additional information provided by the H I here. In fact, besides NGC 4191, there are 16 other ATLAS^{3D} galaxies for which we can compare JAM stellar kinematic inclinations to the kinematic data from large H I discs (den Heijer et al. 2015). Five of the 17 have H I inclinations that are more than 40° different from their stellar JAM inclinations.⁵ Some of these differences may reflect uncertainties in the stellar kinematic modeling as their JAM fits are described as poor quality, but others may reflect real warps and/or misaligned dark matter halos.

7.4 Dynamics at large radii

Aside from the inclination issue, though, the H I dynamics in NGC 4191 are consistent with the stellar dynamics. The deprojected H I circular velocity, 202_{-14}^{+18} km s⁻¹, compares favorably to the Tully-Fisher relation in den Heijer et al. (2015) and to other dynamical relations found for early-type galaxies (Serra et al. 2016, hereafter S16). Given the measured stellar dispersion $\sigma_e = 124$ km s⁻¹ \pm 5 km s⁻¹ (Cappellari et al. 2013), the H I circular velocity is 1.63 ± 0.12 times σ_e . This value is higher than the typical ratio 1.33 ± 0.16 found by S16 but within the combined uncertainties. The H I circular velocity is also 0.87 ± 0.06 times the maximum circular velocity inferred from the stellar dynamics, which is 232 km s⁻¹ at a radius of $2.4''$; again, the H I velocity is on the high side of the typical ratio 0.73 ± 0.13 but is consistent with the dispersion in measured values. And because the H I rotation speed is approximately constant out to such a large radius, the average logarithmic slope of the total density profile in NGC 4191 is 2.06 ± 0.03 , close to isothermal, as is typical for the galaxies in S16.

Finally, it is also worth noting that the H I disc in NGC 4191 is unusually large for early-type galaxies. We measure the circular velocity out to $250''$ or 47.5 kpc, and for $R_e \approx 15''$ (Cappellari et al. 2013; Krajnović et al. 2013a) that is $16 R_e$. The H I extends even farther, out to 68 kpc, on the North side. Of the 16 H I-rich early-type galaxies studied by den Heijer et al. (2015) and S16, none has an H I velocity measured at a radius beyond 28.2 kpc, so NGC 4191's disc is

at least 50% larger than its nearest competitor in that sense. There are also only two other examples with measured H I rotation velocities at $\sim 15 R_e$. These are NGC 2685 and NGC 3838, and the H I distribution in NGC 3838 is noticeably less relaxed and regular than that of NGC 4191.

The total mass implied by the H I circular velocity in NGC 4191 (202 km s⁻¹ at 47.5 kpc) is $4.5 \times 10^{11} M_\odot$, a factor of 9 larger than the dynamical mass implied by the JAM analysis of Cappellari et al. (2013). The JAM dynamical masses refer to a region of radius $\sim R_e$, so the difference clearly implies large dark matter contents in the outer halo of the galaxy. And again, because of the large radius of the H I disc, this factor of 9 is unusual for H I-rich early-type galaxies. The data in S16 show two other galaxies (NGC 2685 and NGC 5582) whose H I-derived dynamical masses are a factor of 6 larger than their stellar-derived JAM masses. NGC 4191 is even more strongly dark matter-dominated than these. For comparison, the median value in S16 is a factor of 2.2 and the dispersion is similarly a factor of 2.1. Thus, NGC 4191 should provide an interesting case study for dynamical modeling at large radii in an early-type galaxy.

7.5 Discussion: Formation and evolution of NGC 4191 and other 2σ galaxies

Krajnović et al. (2013a) described the surface brightness profile of NGC 4191 as fit by a Sérsic profile of index 3.2 ± 0.2 . Coccato et al. (2015) investigated its structure in more detail and described it as consisting of three components: a bulge, which dominates the surface brightness profile and the stellar velocity field at radii $< 3''$; a large disc, which dominates the surface brightness at radii $> 22''$; and a smaller secondary disc, which dominates the surface brightness and the velocity field at intermediate radii $3'' < r < 22''$. The secondary disc is counterrotating with respect to the other two components, and there is some evidence that its stars are younger. It is estimated to contain one third of the total galaxy luminosity, but since it has younger stars, it has a somewhat smaller percentage ($\sim 20\%$) of the total stellar mass. The H I disc rotates in the same sense as the ionized gas and the secondary stellar component. With these results in mind, we consider models for the formation of galaxies like NGC 4191.

Two general scenarios proposed for the formation of 2σ galaxies involve (1) accretion and (2) mergers (e.g. Crocker et al. 2009; Corsini 2014; Coccato et al. 2015; Mitzkus et al. 2017). Option 1 involves the accretion of retrograde gas (and possibly stars) onto a disc galaxy. Misaligned but roughly retrograde gas should settle into the equatorial plane, and subsequent star formation in that gas would form a coplanar but retrograde stellar disc. Algorry et al. (2014) describe a variant in which a galaxy at the intersection of two cosmic filaments could accrete gas first with one spin, from one dominant filament, and then with the opposite spin (from another filament). Option 2 involves a precisely aligned major merger in which two disc galaxies and their mutual orbit are all roughly coplanar, and at least one of the galaxies' spins is antiparallel to the orbital angular momentum. Just how closely aligned the angular momentum vectors would have to be, in option 2, has been partially explored but not well constrained (Bournaud et al. 2005; Bois et al. 2011).

In the case of NGC 4191, Coccato et al. (2015) support

⁵ NGC 3522, NGC 4203, NGC 4262, NGC 4278, and NGC 4191.

the first option on the grounds that they claim tentative evidence for a radial age gradient in NGC 4191, and they propose that a major merger (as in option 2) would erase such gradients. It would probably be worthwhile to check the question more quantitatively since [Bois et al. \(2011\)](#) find that the discy structure of the larger progenitor can be preserved mostly intact in an aligned merger of this type. In any case, the large HI disc in NGC 4191 certainly could be evidence of the accreted retrograde gas. It is worth noting that the present gas mass, $5 \times 10^9 M_{\odot}$ including helium, is smaller than the value that [Coccatto et al. \(2015\)](#) have estimated for the retrograde stellar disc ($\sim 10^{10} M_{\odot}$). The CO nondetection also implies a molecular mass $< 10^8 M_{\odot}$ ([Young et al. 2011](#)). Thus if the HI disc is the remnant of a disc growth phase as in option 1 above, the original mass of accreted gas must have been several times larger than the current gas mass. In fact the mass of accreted gas would probably have been similar to the stellar mass of the galaxy at the time.

Taking a broader view, we note that the configuration in NGC 4191, where the cold gas is rotating in the same sense as the disc with the smaller scale length, is apparently the most common configuration for 2σ early-type galaxies with cold gas. In the ATLAS^{3D} sample 11 examples of 2σ galaxies were identified ([Krajnović et al. 2011](#)), and three of them have cold gas with interferometric maps. These are IC 0719 ([Alatalo et al. 2013](#)), NGC 4550 ([Crocker et al. 2009](#)), and NGC 4191. Beyond ATLAS^{3D}, NGC 5102 is also an early-type 2σ galaxy with cold gas ([Mitzkus et al. 2017](#)). Three of these four cases match the configuration in NGC 4191.⁶ The outlier is NGC 4550, which is found to have two discs of similar scale lengths but different scale heights, and where the molecular and ionized gas rotate like the thicker disc. [Crocker et al. \(2009\)](#) support the merger interpretation (option 2 above) for NGC 4550 and provide a numerical simulation to justify its feasibility. If the configuration found in the other three or four cases can be associated with the accretion scenario (option 1 above), then these data suggest that the accretion scenario is the more common formation pathway for 2σ galaxies. It could also be the case that there is an observational bias, such that 2σ galaxies are easier to detect when the counterrotating disc is younger and brighter, as might be associated with the accretion scenario.

The 2σ galaxies may also be extreme examples of the general phenomenon of gas accretion and disc growth in early-type galaxies. The SAURON and ATLAS^{3D} surveys contain several other cases of fast rotators that host compact kinematically decoupled cores (KDCs), and in some of these cases there is also good evidence that the KDCs may have grown out of accreted gas. Here we consider NGC 3032 and NGC 4150 ([McDermid et al. 2006](#); [Young et al. 2008](#); [Lucero & Young 2013](#); [Oosterloo et al. 2010](#); [Morganti et al. 2006](#)). In NGC 3032 the sense of rotation of the molecular and atomic gas matches that of the young stellar KDC, and it is retrograde with respect to the large-scale stellar

disc. In NGC 4150 the cold gas rotates in the same sense as the large-scale stellar disc, and it is therefore the opposite sense to that of the young stellar KDC; this case is confusing and still poorly understood, and it may involve two separate episodes of accretion. However NGC 3032 might be an example of an early-stage modest 2σ galaxy, where most of the accreted, retrograde gas is still in molecular and atomic form. There are several other cases in ATLAS^{3D} with retrograde gas ([Davis et al. 2013](#)), but the quantity of cold gas is usually not large enough to make a stellar disc with more than a few percent of the total stellar mass. Thus, as discussed above for NGC 4191 specifically, if the 2σ galaxies represent cases of disc growth from accreted retrograde gas, they would require extreme accretion events much more massive than the recent ones. The scenario could potentially be tested in cosmological simulations with large volumes and accurate treatment of gas cooling.

8 SUMMARY

We present new VLA HI observations of 5 ATLAS^{3D} slow rotator early-type galaxies, plus newly reduced archival data on 4 others. Three other ATLAS^{3D} fast rotators are also present in the observed fields along with numerous spirals and dwarf galaxies, and we find one HI cloud without an apparent optical counterpart. With these new data, 34 of the 36 ATLAS^{3D} slow rotators now have sensitive HI observations at arcminute-scale resolution (4 to 10 kpc) from either WSRT, the VLA, or Arecibo. Typical column density limits are about $2.5 \times 10^{19} \text{ cm}^{-2}$, and typical mass limits are a few $10^7 M_{\odot}$ of HI.

The ATLAS^{3D} survey is the first large, volume-limited survey of stellar kinematics in early-type galaxies. Thus it provides the best opportunity to make the connections between the galaxies' histories, as recorded in their stellar kinematics, with their histories as recorded in their cold gas. The new observations also add to what is known about the diversity of HI in slow rotators, as the two new detections are unusual for slow rotators.

The new data enable a more complete assessment of the HI properties of slow and fast rotators; in general, they reinforce the similarities between the HI of the two types. The HI detection rates are entirely consistent with each other. All of the HI morphological types (small discs, large discs, isolated clouds and unsettled distributions) are now known to be present in both slow and fast rotators. The two new HI detections discussed here also have very large HI contents, giving $M(\text{HI})/M_{\star} \sim 0.1$, which is nearly as high as the most gas-rich fast rotators. As expected, these HI-rich slow rotators are found in low density environments. And since the slow and fast rotators probably had very different formation paths ([Cappellari 2016](#)), the fact that their HI properties are very similar suggests that their current HI properties are more a reflection of their recent accretion/interaction history than their high- and moderate-redshift formation events.

One interesting deviation from the previous picture is that the new HI detections have their HI kinematics well aligned with their stellar kinematics. Earlier detections of relaxed HI discs in slow rotators were in roughly polar configurations, with the HI kinematic axis 90° out from the stellar kinematic axis. [S14](#) commented that it was difficult

⁶ Additional observations of NGC 4476 from the PPAK IFU at Calar Alto show that this galaxy is also a 2σ galaxy and the field of view of the SAURON instrument is slightly too small to show the counterrotation. NGC 4476 also fits the pattern where the cold and ionized gas rotate like the inner stellar disc ([Crocker 2009](#)). If NGC 4476 is included, then four of the five cases with cold gas maps match the configuration in NGC 4191.

for their simulations to produce so many polar gas discs. The new detections alleviate that difficulty to some extent, though they do not eliminate it. In these senses the new H I data broaden the known diversity of H I properties in slow rotators, and it would be useful to re-examine the H I properties of simulated slow rotators.

NGC 1222, one of the two slow rotators that we discuss in some detail, is a starbursting merger remnant. Its stellar body shows prolate-like rotation and the H I occurs in a moderate-inclination disc, with its kinematic axis roughly aligned with the stars and the ionized gas. If the galaxy is indeed prolate, the H I is in its equatorial plane. NGC 1222 also shows shells and tidal tails, evidence of the recent merger; no H I is found associated with the shells or tails, so deeper H I observations would be necessary to tell whether the merger was gas-rich or whether perhaps the gas was accreted later. The question is interesting in the light of simulation work probing the origins of prolate-like rotation and prolate shapes (Li et al. 2018; Tsatsi et al. 2017; Ebrova & Lokas 2017).

The other slow rotator discussed in detail is NGC 4191, a “2 σ -peak” galaxy made of two coplanar but counterrotating stellar discs. We find that it has an unusually large H I disc of diameter greater than 100 kpc, which allows us to measure a dynamical mass out to 16 R_e . The H I shows a mild kinematic twist but there is a large discrepancy between the $\sim 45^\circ$ inclination inferred from H I and ionized gas and the $\sim 90^\circ$ inclination inferred from an axisymmetric stellar dynamical model. Inclinations aside, the H I disc rotates in the same sense as the smaller and more compact of the two stellar discs, so it is retrograde with respect to the primary stellar disc. This configuration is found in three of the four 2σ galaxies with the appropriate data. Accretion-driven disc growth might explain the retrograde gas and stellar disc in NGC 4191, though more detailed simulations of the aligned merger model should also be carried out. There is abundant evidence for misaligned cold gas accretion in the ATLAS^{3D} sample, but NGC 4191 has the largest cold gas mass of these cases.

In any discussion of slow rotators it is useful to keep in mind that there is some argument for removing the 2σ galaxies like NGC 4191 from the slow rotator class (e.g. Cappellari 2016). We have retained the 2σ galaxies in the discussion here simply because of their past classifications.

In general, because the early-type galaxies are relatively poor in cold gas, their cold gas properties provide sensitive benchmarks for numerical simulations of galaxy evolution. Their diversity in gas content and in gas kinematics stands in striking contrast to the properties of spirals, and therefore the early-type galaxies provide a greater challenge to the simulations that include cold gas (e.g. Serra et al. 2014; Lagos et al. 2015).

ACKNOWLEDGMENTS

Thanks to L. Coccato for providing the [O III] data from their paper, and to Alison Crocker and Gareth C. Jones for helpful discussions.

The National Radio Astronomy Observatory is a facility of the National Science Foundation operated under cooperative agreement by Associated Universities, Inc. This

research has made use of the NASA/IPAC Extragalactic Database (NED) which is operated by the Jet Propulsion Laboratory, California Institute of Technology, under contract with the National Aeronautics and Space Administration. We acknowledge the usage of the HyperLeda database (<http://leda.univ-lyon1.fr>).

REFERENCES

- Alatalo K., et al., 2013, *MNRAS*, **432**, 1796
 Algorry D. G., Navarro J. F., Abadi M. G., Sales L. V., Steinmetz M., Piontek F., 2014, *MNRAS*, **437**, 3596
 Bois M., et al., 2011, *MNRAS*, **416**, 1654
 Boizelle B. D., Barth A. J., Darling J., Baker A. J., Buote D. A., Ho L. C., Walsh J. L., 2017, *ApJ*, **845**, 170
 Boselli A., Cortese L., Boquien M., 2014, *A&A*, **564**, A65
 Bournaud F., Jog C. J., Combes F., 2005, *A&A*, **437**, 69
 Brauer J. R., Dale D. A., Helou G., 2008, *ApJS*, **178**, 280
 Cappellari M., 2016, *ARA&A*, **54**, 597
 Cappellari M., et al., 2011a, *MNRAS*, **413**, 813
 Cappellari M., et al., 2011b, *MNRAS*, **416**, 1680
 Cappellari M., et al., 2013, *MNRAS*, **432**, 1709
 Coccato L., et al., 2015, *A&A*, **581**, A65
 Condon J. J., Cotton W. D., Greisen E. W., Yin Q. F., Perley R. A., Taylor G. B., Broderick J. J., 1998, *AJ*, **115**, 1693
 Corsini E. M., 2014, in Iodice E., Corsini E. M., eds, *Astronomical Society of the Pacific Conference Series Vol. 486, Multi-Spin Galaxies*. p. 51 ([arXiv:1403.1263](https://arxiv.org/abs/1403.1263))
 Cortese L., et al., 2016, *MNRAS*, **459**, 3574
 Courtois H. M., Tully R. B., 2015, *MNRAS*, **447**, 1531
 Crocker A. F., 2009, PhD thesis, University of Oxford
 Crocker A. F., Jeong H., Komugi S., Combes F., Bureau M., Young L. M., Yi S., 2009, *MNRAS*, **393**, 1255
 Davis T. A., et al., 2011, *MNRAS*, **417**, 882
 Davis T. A., et al., 2013, *MNRAS*, **429**, 534
 Davis T. A., et al., 2014, *MNRAS*, **444**, 3427
 Di Teodoro E. M., Fraternali F., 2015, *MNRAS*, **451**, 3021
 Doyle M. T., et al., 2005, *MNRAS*, **361**, 34
 Duc P.-A., et al., 2011, *MNRAS*, **417**, 863
 Duc P.-A., et al., 2015, *MNRAS*, **446**, 120
 Duprie K., Schneider S. E., 1996, *AJ*, **112**, 937
 Dwarakanath K. S., van Gorkom J. H., Owen F. N., 1994, *ApJ*, **432**, 469
 Ebrova I., Lokas E. L., 2017, preprint, ([arXiv:1708.03311](https://arxiv.org/abs/1708.03311))
 Emsellem E., et al., 2011, *MNRAS*, **414**, 888
 Giovanelli R., et al., 2005, *AJ*, **130**, 2598
 Haynes M. P., et al., 2011, *AJ*, **142**, 170
 Huchtmeier W. K., Richter O.-G., 1989, *A General Catalog of HI Observations of Galaxies. The Reference Catalog*.
 Janowiecki S., et al., 2015, *ApJ*, **801**, 96
 Jedrzejewski R. I., 1987, *MNRAS*, **226**, 747
 Krajnović D., Cappellari M., de Zeeuw P. T., Copin Y., 2006, *MNRAS*, **366**, 787
 Krajnović D., et al., 2011, *MNRAS*, **414**, 2923
 Krajnović D., et al., 2013a, *MNRAS*, **432**, 1768
 Krajnović D., et al., 2013b, *MNRAS*, **433**, 2812
 Lagos C. d. P., Padilla N. D., Davis T. A., Lacey C. G., Baugh C. M., Gonzalez-Perez V., Zwaan M. A., Contreras S., 2015, *MNRAS*, **448**, 1271
 Lagos C. d. P., Theuns T., Stevens A. R. H., Cortese L., Padilla N. D., Davis T. A., Contreras S., Croton D., 2017, *MNRAS*, **464**, 3850
 Li H., Mao S., Emsellem E., Xu D., Springel V., Krajnović D., 2018, *MNRAS*, **473**, 1489
 Lim J., Ao Y., Dinh-V-Trung 2008, *ApJ*, **672**, 252
 Lucero D. M., Young L. M., 2013, *AJ*, **145**, 56

- Lucero D. M., Young L. M., van Gorkom J. H., 2005, *AJ*, **129**, 647
- McConnachie A. W., 2012, *AJ*, **144**, 4
- McDermid R. M., et al., 2006, *MNRAS*, **373**, 906
- Mitzkus M., Cappellari M., Walcher C. J., 2017, *MNRAS*, **464**, 4789
- Morganti R., et al., 2006, *MNRAS*, **371**, 157
- Mundell C. G., et al., 2007, *New Astron. Rev.*, **51**, 34
- Negri A., Pellegrini S., Ciotti L., 2015, *MNRAS*, **451**, 1212
- Ogle P., Boulanger F., Guillard P., Evans D. A., Antonucci R., Appleton P. N., Nesvadba N., Leipski C., 2010, *ApJ*, **724**, 1193
- Oosterloo T., et al., 2010, *MNRAS*, **409**, 500
- Russell H. R., et al., 2017, *MNRAS*, **472**, 4024
- Schiminovich D., van Gorkom J. H., van der Hulst J. M., Kasow S., 1994, *ApJ*, **423**, L101
- Schiminovich D., van Gorkom J. H., van der Hulst J. M., Malin D. F., 1995, *ApJ*, **444**, L77
- Schiminovich D., van Gorkom J. H., van der Hulst J. M., 2013, *AJ*, **145**, 34
- Serra P., et al., 2012, *MNRAS*, **422**, 1835
- Serra P., et al., 2014, *MNRAS*, **444**, 3388
- Serra P., Oosterloo T., Cappellari M., den Heijer M., Józsa G. I. G., 2016, *MNRAS*, **460**, 1382
- Smith M. W. L., et al., 2012, *ApJ*, **748**, 123
- Sparke L. S., 1996, *ApJ*, **473**, 810
- Temi P., Amblard A., Gitti M., Brighenti F., Gaspari M., Mathews W. G., David L., 2017, preprint, ([arXiv:1711.10630](https://arxiv.org/abs/1711.10630))
- Thomas H. C., Dunne L., Green D. A., Clemens M. S., Alexander P., Eales S., 2004a, *MNRAS*, **348**, 1197
- Thomas H. C., Alexander P., Clemens M. S., Green D. A., Dunne L., Eales S., 2004b, *MNRAS*, **351**, 362
- Tsatsi A., Lyubenova M., van de Ven G., Chang J., Aguerri J. A. L., Falcón-Barroso J., Macciò A. V., 2017, preprint, ([arXiv:1707.05130](https://arxiv.org/abs/1707.05130))
- Weijmans A.-M., et al., 2014, *MNRAS*, **444**, 3340
- Werner N., et al., 2014, *MNRAS*, **439**, 2291
- Wilson C. D., et al., 2013, *ApJ*, **776**, L30
- Young L. M., Bureau M., Cappellari M., 2008, *ApJ*, **676**, 317
- Young L. M., et al., 2011, *MNRAS*, **414**, 940
- Young L. M., et al., 2014, *MNRAS*, **444**, 3408
- den Heijer M., et al., 2015, *A&A*, **581**, A98
- van de Voort F., Davis T. A., Kereš D., Quataert E., Faucher-Giguère C.-A., Hopkins P. F., 2015, *MNRAS*, **451**, 3269

APPENDIX A: OTHER H I DETECTIONS

Several other galaxies in the vicinity of our targets are also detected in H I emission. Basic properties are given in Table A1; overlays on the optical images are also shown in Figures 4, B1, and B4, and spectra are in Figures B2, B3, and B5. In the case of the NGC 5846 group mosaic, it is worth noting that the large spiral NGC 5850 is also in the mosaic field but falls outside of the velocity range covered, so it is not detected. Several of the detected galaxies also have previously published H I fluxes, primarily from the Arecibo and Parkes telescopes, but some appear to be new H I detections. The spatial resolution of the VLA data is much better than previous single-dish data (e.g. about a factor of 4 better than Arecibo), so the H I positions are correspondingly better. In some cases the resolution also allows us to estimate kinematic position angles.

The H I properties we measure for NGC 5806, NGC 5811, UGC 09661, and NGC 5577 are all consistent with measurements published elsewhere, with one exception. The H I line flux we measure for NGC 5806 is almost a factor of two lower than previous single-dish measurements. The discrepancy is undoubtedly due to the source being beyond the half-power point of the VLA primary beam. The relevant pixels have been multiplied up by factors of 3 to 5 to account for the primary beam gain, but the imaging quality is still poor that far out. For this source, there are better VLA C configuration data with NGC 5806 at the pointing center (Mundell et al. 2007).

PGC 1218738, PGC 1215798, PGC 1180802, PGC 1211621, and AGC 249460 do not have H I detections formally published elsewhere, but they are listed in the ALFALFA survey data in the first-release version $\alpha.100$ “A grids” data files.⁷ Again, the H I properties measured here are consistent with the single-dish detections, except for PGC 1211621. In this case the H I emission is found up to the very last usable channel in the VLA data cube, and it may well extend beyond that. The flux measured here is a lower limit for that reason.

UGC 07945, PGC 054045, and PGC 1190358 do not have any other published H I fluxes, to the best of our knowledge. UGC 07945 is outside of the ALFALFA survey area, and the other two are nominally covered by the ALFALFA survey but their flux is near or below the typical detection limit (Haynes et al. 2011).

APPENDIX B: AN INTRIGUING ISOLATED H I CLOUD

AGC 249460 and the NGC 5574–5576–5577 group (Figure 4) merit further discussion. NGC 5576, NGC 5574, and NGC 5577 form a compact triple with projected separations $< 200 \text{ km s}^{-1}$ and ~ 20 and 70 kpc , and the deep image of Duc et al. (2015) shows dramatic evidence of an advanced interaction between NGC 5574 and NGC 5576. However, NGC 5577 appears undisturbed both in the optical image and in H I emission, so its physical separation from the other two must be much larger. Another possible member of the

group, AGC 249460, is identified as an H I source in the ALFALFA $\alpha.100$ catalog but an optical counterpart has not yet been identified. This makes it an unusual H I-rich object, as we will discuss in further detail below.

From the VLA image we estimate the centroid of AGC 249460 to be located at $14^{\text{h}} 20^{\text{m}} 07.721^{\text{s}}$, $03^{\circ}27'42.761''$ (J2000), with a positional uncertainty of about $1.5''$ in each direction. This position is $23''$ east of the one quoted in the ALFALFA catalog, but that is consistent with the Arecibo positional uncertainties. We assume a distance of 24.5 Mpc , based on association with NGC 5577, which means the H I flux corresponds to a mass of $1.3 \times 10^8 M_{\odot}$ or $1.7 \times 10^8 M_{\odot}$ including helium. Most unusually, the MATLAS image shows no extended optical counterpart at its location, with a limiting surface brightness in g of $28.5 \text{ mag/arcsec}^2$.

B1 Mass and luminosity

For an analysis of the physical properties of AGC 249460, it is instructive to compare it to other optically faint ALFALFA detections that have similar H I fluxes and assumed distances. Three such objects are discussed by Janowiecki et al. (2015); one of them has a faint optical counterpart of about $15''$ (1.8 kpc) radius, and if we adopt that same radius here for AGC 249460 we find that its integrated magnitude must be fainter than -10.7 in g . Its luminosity is thus $L_g < 2.2 \times 10^6 L_{\odot}$ and its H I mass gives an extremely large $M(\text{H I})/L_g > 60$. The H I mass is similar to the most gas-rich dwarf galaxies of the Local Group, such as NGC 6822, but the optical luminosity is similar to that of the faint dwarf spheroidals (e.g. McConnachie 2012). Thus, the source has no direct analog in the Local Group, and because of the fainter surface brightness limit, it has even more extreme $M(\text{H I})/L$ ratios than the other objects discussed by Janowiecki et al. (2015). This object may be one of the “darkest” of the dark (optically faint) galaxies.

The H I emission in AGC 249460 is not well resolved, so dynamical mass estimates have a large uncertainty, but they do help constrain the nature of the object. A Gaussian fit to the integrated line profile gives a velocity dispersion of $11.0 \pm 1.3 \text{ km s}^{-1}$. A 2D Gaussian fit to the column density gives an estimated *deconvolved* size of ($43'' \pm 9''$) by ($33'' \pm 11''$) FWHM, so a radius of $20'' = 2.4 \text{ kpc}$ may be reasonable. These values give a virial mass estimate of $2.7 \times 10^8 M_{\odot}$, which is only modestly larger than the known atomic gas mass of $1.7 \times 10^8 M_{\odot}$. Thus, the data suggest that AGC 249460 is gravitationally bound, but it's not clear whether it requires a large dark matter component. AGC 249460 could be a tidal dwarf galaxy with very little dark matter. It certainly does not have a dominant stellar component, and it's not entirely clear why there hasn't been much star formation. The peak column density in these data is $2.1 \times 10^{20} \text{ cm}^{-2}$, which suggests that at higher resolution the H I may be thick enough to form H_2 .

We note also that the estimated virial/gas mass ratio would be larger if the object's actual distance is substantially less than the 24.5 Mpc we have assumed, and in that case the evidence for dark matter would be stronger; but at the moment there is no other evidence against the association with the NGC 5574–5576–5577 group.

⁷ <http://egg.astro.cornell.edu/alfalfa/data/index.php>

Table A1. Other H I detections.

Name	Dist. (Mpc)	Primary Target	H I flux (Jy km s ⁻¹)	H I mass (M _⊙)	Offset (′)	PB gain	Kin. PA (deg)
(1)	(2)	(3)	(4)	(5)	(6)	(7)	(8)
NGC 5806	21.4	NGC 5813	5.9 (0.5)	6.4×10 ⁸	21	0.19 – 0.33	174 (3)
NGC 5811	20?	NGC 5813	1.07 (0.06)	1.0×10 ⁸	12	0.63 – 0.73	–85 (30)
UGC 09661	20?	NGC 5813	2.4 (0.1)	2.3×10 ⁸	15	0.44 – 0.56	234 (10)
UGC 07945	40?	NGC 4690	2.0 (0.1)	7.6×10 ⁸	14	0.62 – 0.51	–81 (5)
NGC 5577	24.5	NGC 5576	11.0 (0.2)	1.6×10 ⁹	11	0.67 – 0.83	67 (1)
AGC 249460	24.5?	NGC 5576	0.9 (0.1)	1.3×10 ⁸	18	0.39	...
PGC 1218738	24?	NGC 5838/5846 group	0.82 (0.09)	1.1×10 ⁸	–16 (11)
PGC 1215798	24?	NGC 5838/5846 group	3.91 (0.17)	5.3×10 ⁸	26 (3)
PGC 1180802	24?	NGC 5831/5846 group	1.44 (0.14)	2.0×10 ⁸	67 (12)
PGC 054045	24?	NGC 5846	0.28 (0.07)	3.8×10 ⁷
PGC 1190358	24?	NGC 5831/5846 group	0.31 (0.06)	4.2×10 ⁷
PGC 1211621	24?	NGC 5838/5846 group	0.21 (0.03)	2.8×10 ⁷

Distances are taken from Cappellari et al. (2011a), though those marked with ‘?’ are estimated by association or from a Hubble flow calculation. The primary target in column 3 indicates the nearest ATLAS^{3D} galaxy and the dataset in which the object is found. For the objects observed with a single pointing, the offset in column 6 describes the distance from the pointing center to the object, and the primary beam gain over the region of interest (possibly a range, due to the finite source size) is in column 7. The offset information is included to give a rough indication of the imaging quality and the uncertainties in the measured fluxes. It is difficult to be precise, but uncertainties of 20% or more may be reasonable for objects beyond the half-power point of the primary beam (radius $\sim 15.5'$). The kinematic position angle in column 8 is defined from North towards East to the *receding* side of the galaxy, and it is quantified from the first velocity moment image as in Krajnović et al. (2006).

B2 Origin

Considering the origin of AGC 249460 and the suggestion that it might be a tidal dwarf, we note the obvious interaction between NGC 5574 and NGC 5576 (Figure 4). But the orientation of NGC 5574’s tail suggests that alteration is not relevant for AGC 249460.

Thus, we consider whether AGC 249460 could be gas stripped from NGC 5577, the only other galaxy in the vicinity that still has HI. Any presumed interaction must have been weak or happened a significant time ago, so that the HI in NGC 5577 should currently appear undisturbed. For comparison, the orbital time at the outer edge of the HI disc in NGC 5577 is 300 Myr. The projected distance between the objects is 16′ or 110 kpc, and the time required to travel that distance at 300 km s⁻¹ is 360 Myr. The observed velocity difference between the two is only 10 km s⁻¹, though, so that if we presume a strong interaction then AGC 249460 must be at very nearly the same distance as NGC 5577. (If it is significantly in front of or behind then the crossing time in the radial direction at 10 km s⁻¹ becomes very long.)

NGC 5577 itself shows possible signs of being stripped; Boselli et al. (2014) give it an HI deficiency of 0.52 dex compared to its “normal” analogs. Furthermore, its HI mass and *B* luminosity give $M(\text{HI})/L_B \sim 0.16 M_{\odot}/L_{\odot}$, which is unusually low for spirals (e.g. Janowiecki et al. 2015). The maximum radius of its HI, as measured from the centroids of emission at the extreme velocities, is 50″ or only 5.9 kpc.

All of this evidence is broadly consistent with a picture in which AGC 249460 could have been a small amount of matter stripped from NGC 5577. It could also be an unrelated dwarf galaxy which simply didn’t have much star formation. In either case, the faintness of its optical companion makes it worthy of additional study.

This paper has been typeset from a T_EX/L^AT_EX file prepared by the author.

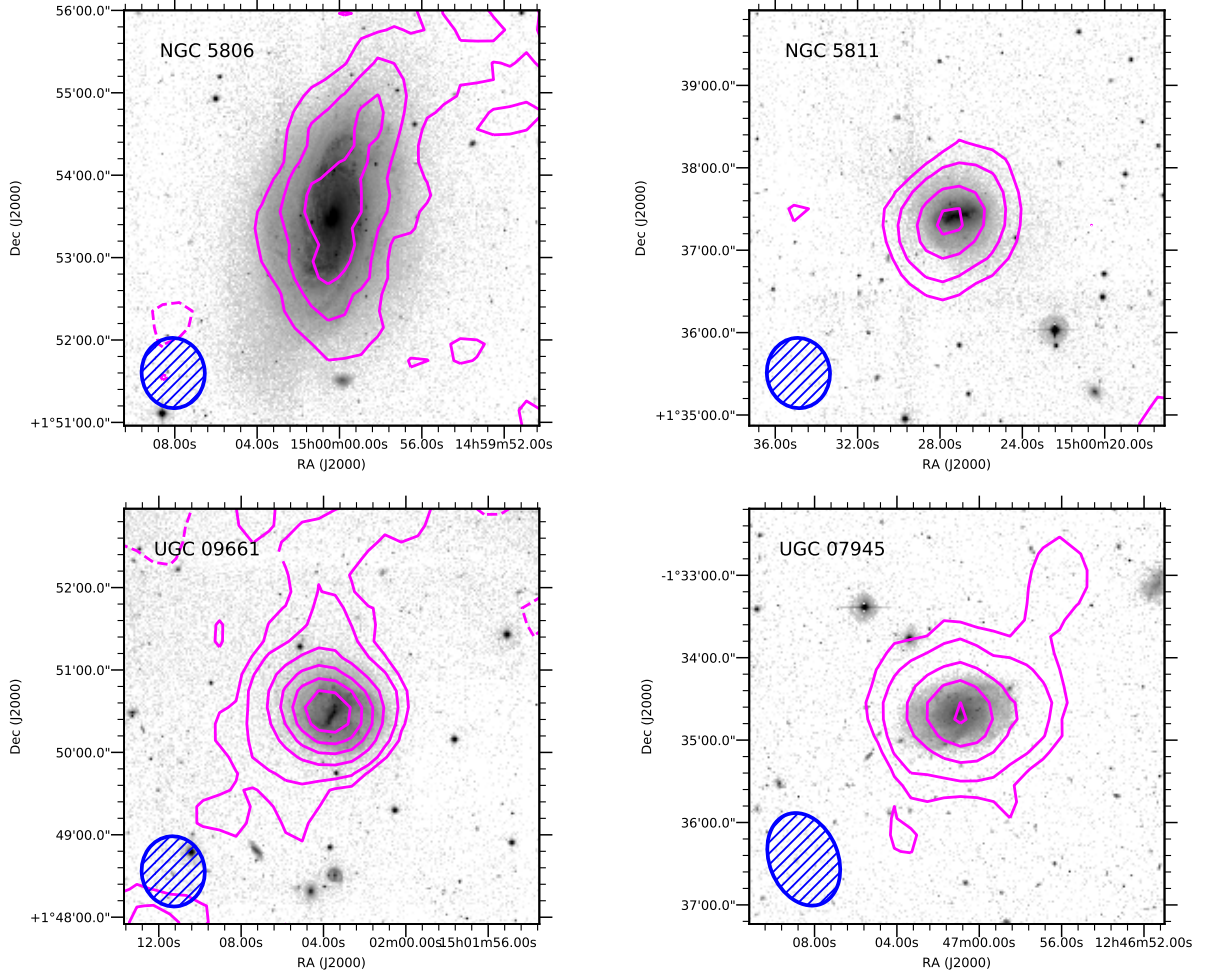


Figure B1. H I and optical images of other detections in the fields of NGC 5813 and NGC 4690. The optical images are MATLAS *g*. The H I column density contours are overlaid; contour levels are $(-0.5, 0.5, 1, 2, 3, 4, 5) \times 10^{20} \text{ cm}^{-2}$, except for NGC 5806, where they are $(-2, 2, 4, 6) \times 10^{20} \text{ cm}^{-2}$. The beam size is indicated in the bottom left corner. Contours extending off the edges of the images are not believed to indicate real emission, but are probably indicative of noise amplified by the primary beam correction.

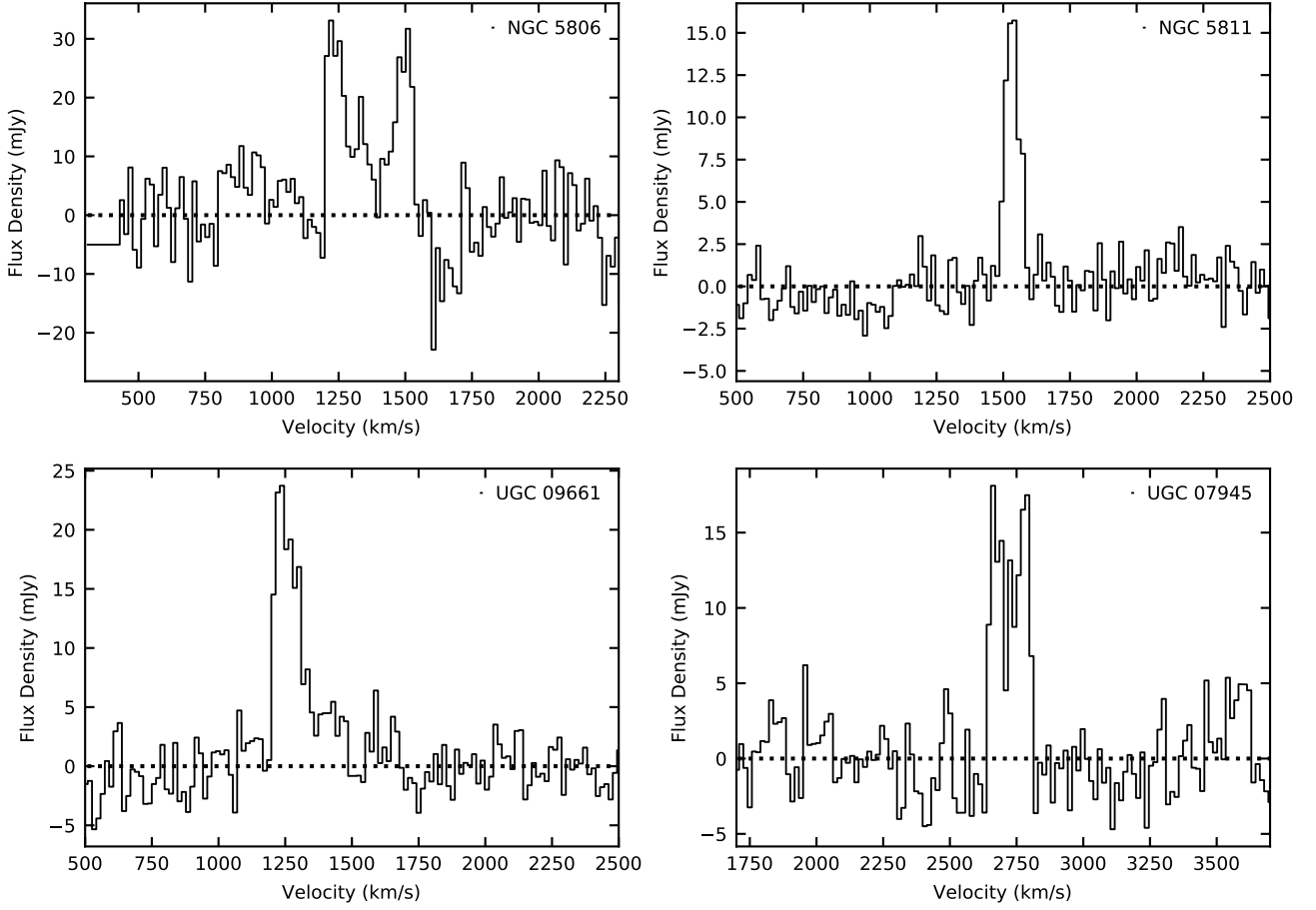


Figure B2. HI spectra for the galaxies in Figure B1. Spectra are constructed by using the integrated intensity to define a spatial region, and then integrating the primary beam-corrected data cube within that same spatial region for all velocities. HI fluxes are measured from the spectra, using the rms in the spectrum and the number of channels with emission to define the uncertainty in the HI flux.

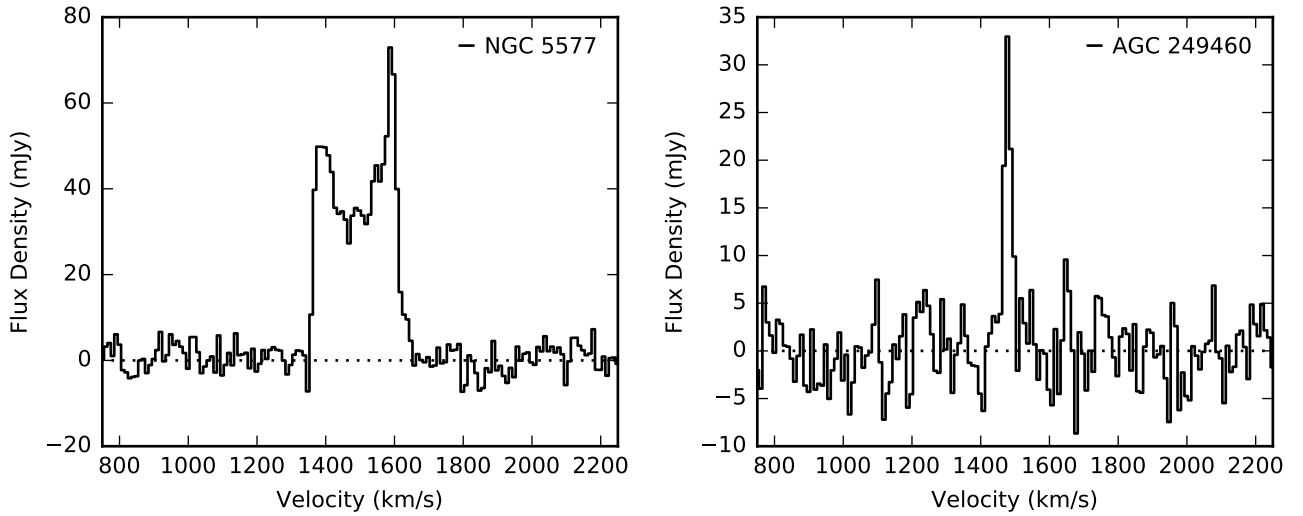


Figure B3. Spectra of NGC 5577 and AGC 249460. (The integrated intensity images are in Figure 4.)

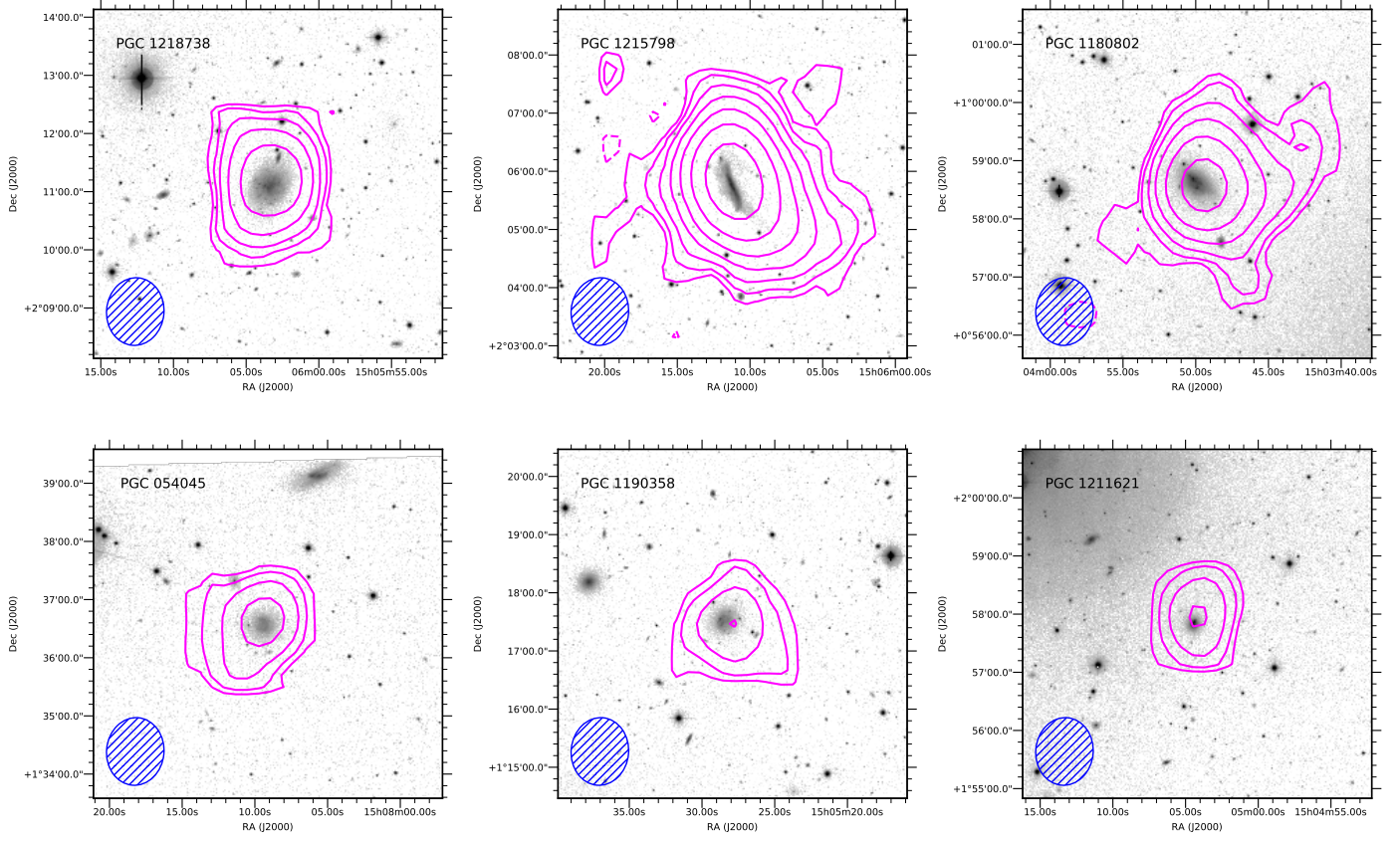


Figure B4. H I-detected galaxies in the NGC 5846 group. Contour levels are $(-0.5, 0.5, 1, 2, 4, 8, 16, 32) \times 1.3 \times 10^{19} \text{ cm}^{-2}$. The optical image is the MATLAS g data, except for PGC 054045, where it is SDSS g .

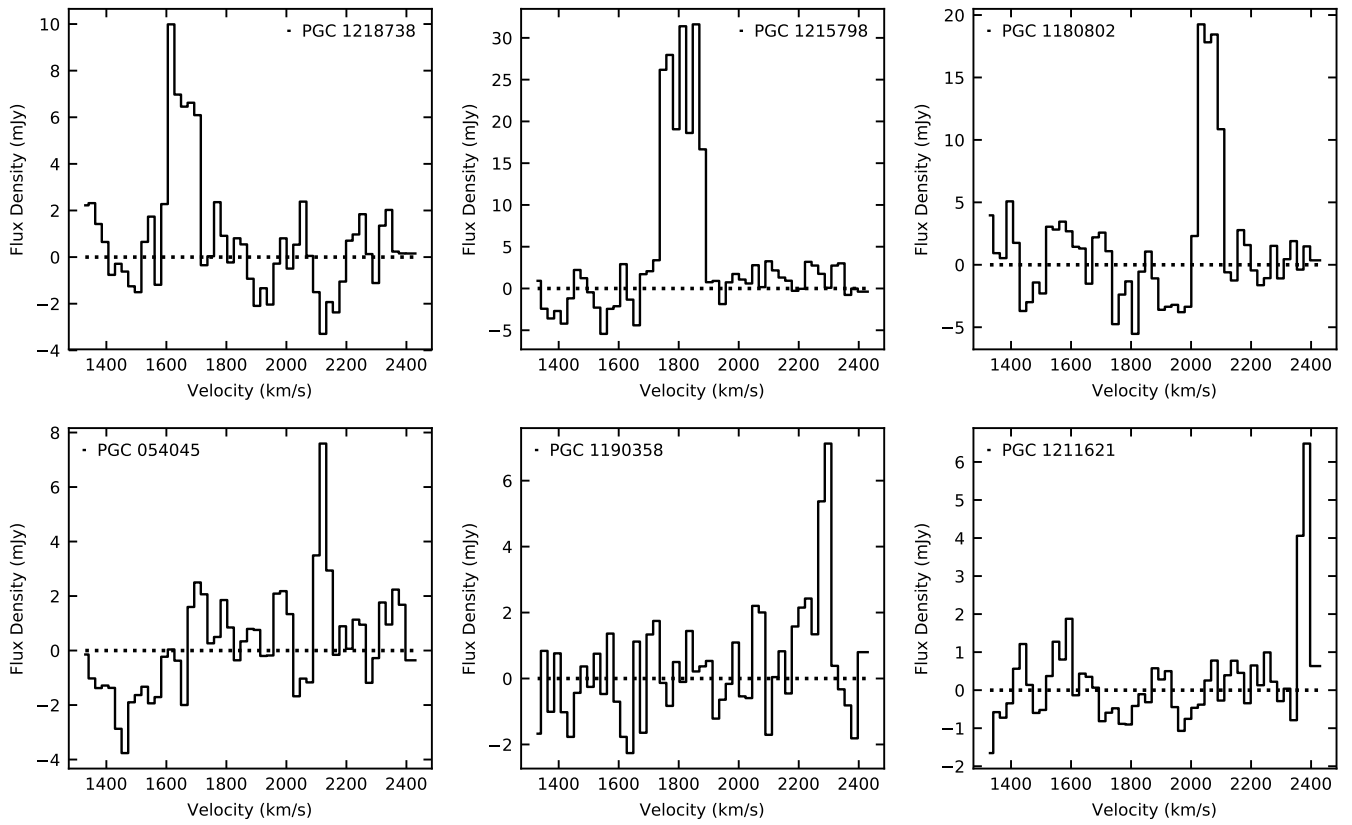


Figure B5. Spectra of H I-detected galaxies in the NGC 5846 group.